Thesis Report:

T-H-M Modelling of gas migration between boreholes in bedded rock salt; simulating argon flow cessation during heating in the Brine Availability Test in Salt (BATS-2g; Decovalex 2027)

Sophie de Nonancourt (097766, Utrecht University)

1st Supervisor: Dr Fred Beekman (Utrecht University)

2nd (daily) Supervisor: Dr Jeroen Bartol (COVRA N.V.)

Submitted on the 17th of July, 2026

Abstract

Gas migration between boreholes in bedded rock salt is an uncertainty in assessing the safety of deep geological repositories for radioactive waste. This thesis introduces a three-dimensional thermo-hydro-mechanical (THM) model of the Brine Availability Test in Salt phase II (BATS-2g) experiment at the Waste Isolation Pilot Plant (WIPP), New Mexico. The work is part of the DECOVALEX 2027 program and the Dutch COPERA research initiative of COVRA. Built in COMSOL Multiphysics 6.4, the model simulates argon gas migration between a central heater borehole (HP) and a source borehole (D), which are connected by a single fracture in an impermeable rock salt matrix. When the heater is activated, argon flow stops within about 70 minutes. Thermoelastic expansion of the salt produces compressive stresses that are strongest near the HP end of the fracture, where heating is most intense. This reduces transmissivity and forms a bottleneck, cutting off hydraulic connectivity between the two boreholes before the fracture fully closes. After heating, the large pressure drop seen in experiments cannot be explained by fracture reopening alone. Instead, it likely results from the collective reopening of a network of microfractures within the excavation-damaged zone (EDZ) under cooling-induced tensile stresses. The main limitations of the model are that it does not include viscoplastic creep, poroelastic coupling, or dilatancy. Addressing these is a priority for future work in the COPERA and DECOVALEX programs.

1. Introduction

1.1. Nuclear energy, radioactive waste and the Dutch context

Radioactive waste in the Netherlands is generated by commercial nuclear power production, medical radioisotope manufacturing, and various industrial applications. The Borssele nuclear power station in Zeeland, operational since 1973, currently supplies approximately 3% of the nation's electricity (COVRA, 2025). Two research reactors are also in operation: the High Flux Reactor (HFR) at Petten, which produces medical radioisotopes for cancer diagnostics and treatment, and a reactor at the Technical University of Delft, which supports educational and materials research activities (COVRA, 2025). In December 2024, the Dutch government announced plans to construct four additional commercial reactors by 2035 as part of its national energy transition strategy (Ministry of Climate and Green Growth, 2024). This planned expansion of the nuclear sector is expected to increase the volume of radioactive material requiring secure, permanent disposal.

Even without future nuclear expansion, the current inventory also needs long-term management. All radioactive waste generated in the Netherlands is currently stored in an interim surface storage facility at the Centrale Organisatie Voor Radioactief Afval (COVRA N.V.) facility in Nieuwdorp, Zeeland (COVRA, 2025). Because a significant fraction of this inventory remains hazardous for millennia, surface storage cannot guarantee permanent long-term isolation (Van der Veen et al., 2018; Bartol & Vuorio, 2025). Deep geological disposal is the internationally accepted long-term solution, with nations such as Finland and Sweden currently in the repository construction phase (IAEA, 2011; NEA, 2020).

1.2. Dutch research context: from ICK to COPERA

The Dutch geological-disposal research summarised in this section follows Van der Veen et al. (2018), Bartol & Vuorio (2025), and Ottenheim (2025). Dutch research on geological disposal has been organized, since the early 1970s, as a sequence of national programs alternating in focus between rock salt and clay as candidate host rocks. The Interdepartementale Commissie Kernenergie (ICK; 1972-1979) identified Zechstein rock salt as a candidate for radioactive-waste disposal in the Dutch subsurface. The

Onderzoeksprogramma Lange Afvalopslag (OPLA; 1985-1993) examined in more detail the long-term feasibility of disposal in salt formations.

Rock salt was chosen as a candidate host rock due to its extremely low matrix permeability ($10^{-21} m^2$, equivalent to $\sim 10^{-5}\ mDarcy$), ductile creep deformation that allows fractures to heal, and its resistance to brittle fracturing (Kuhlman et al., 2024; Bartol & Vuorio, 2025). However, these properties are altered within the excavation-damaged zone (EDZ) immediately surrounding drifts or boreholes, where microfracturing increases porosity and permeability while reducing brine saturation (Borns & Stormont, 1988; Kuhlman et al., 2024).

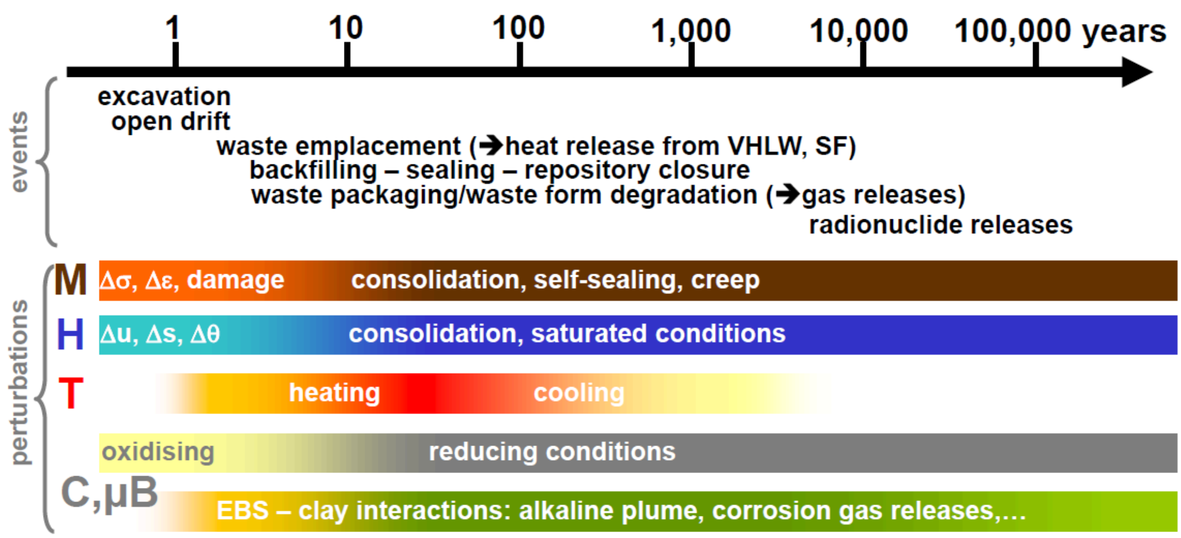

Figure 1. Major thermal (T), hydrological (H), mechanical (M), and chemical (C) perturbations of engineered and natural barriers over the lifetime of a deep geological repository. The timeline spans from excavation and waste emplacement through backfilling and repository closure, to radionuclide releases over timescales up to 100,000 years. The BATS-2g experiment targets early thermal, hydrological, and mechanical perturbations, in which heat-driven T-H-M coupling governs the evolution of fracture permeability in the EDZ (Sillen, HADES Symposium, 2011).

These excavation-induced changes led the Commissie Opberging Radioactief Afval (CORA; 1995-2001) to expand the national research programme to include clay host rocks (Commissie Opberging Radioactief Afval, 2001). This approach was further developed by the Onderzoeksprogramma Eindberging Radioactief Afval (OPERA; 2011-2018), which established a safety case for clay-hosted disposal (Van der Veen et al., 2018). The current national program, COPERA (2020-present), succeeds OPERA and continues research on both rock salt and clay (COVRA, 2025). A main priority for salt research within COPERA is understanding the coupled thermal-hydrological-mechanical (THM) processes triggered when high-level waste releases thermal energy into the host rock (Birkholzer et al., 2024). Temperature variations modify mechanical and hydrological properties, deformation changes fluid flow via fracture opening and closure, and fluid flow redistributes thermal energy (Birkholzer et al., 2024). Coupled THM models are required to quantify these interacting processes (Fig. 1), as radionuclide transport is more likely to occur through the EDZ than through intact salt (Watson et al., 2025). Therefore, understanding these processes is critical for assessing repository safety, as heat-driven gas or fluid migration can create preferential transport pathways and compromise long-term isolation (LaForce et al., 2024).

1.3. The DECOVALEX program, BATS II task and research question

International research on such coupled THM processes in geological systems is coordinated via the DECOVALEX (DEvelopment of COupled models and their VALidation against EXperiments) project, a collaboration between several nuclear waste management organizations and regulatory authorities, currently in its 2024-2027 phase (Birkholzer et al., 2024). To validate different modelling approaches, participating institutions simulate identical tasks using field data, including several salt-focused experiments based on the Waste Isolation Pilot Plant (WIPP) in New Mexico (LaForce et al., 2024). The current experimental phase (DECOVALEX 2027) continues Task E from the previous cycle as BATS 2 (Brine Availability Test in Salt). The task is structured as five sequential steps of increasing complexity (Kuhlman et al., 2024b):

- **Step 0.** Reproducing heat conduction during three heater tests at power levels of 200 W, 400 W, and 500 W, calibrated against experimental temperature data from WIPP (BATS2a through BATS2c).
- **Step 1.** Gas migration through fractured salt between two boreholes (from D to HP) during a later heater test (BATS2g).
    - **a.** Hydraulic modelling of tracer gas migration between boreholes.
    - **b.** Thermomechanical permeability models covering that gas flow stops/starts with heating/cooling.
- **Step 2.** Modelling salt-specific H2O sources (Clay, hydrous minerals, fluid inclusions).

- **Step 3**. BATS 2 responses for different length tests (e, f & g) using steps 1 and 2 developments.
- **Step 4.** Scaling up BATS2 results to repository-scale relevance (cross-collaboration with Salt PA task), including drift-scale EDZ migration of brine, which may be an initial condition for PA models.

Prior modelling by Ottenheim (2025) completed step 0 using a 2D axisymmetric model in COMSOL Multiphysics 6.4, reproducing heat conduction at specific sensor positions and matching inlet pressure decay during the pre-heating gas injection test. This work starts by re-implementing step 0 and extends into steps 1a and 1b.

The principal research question addressed in this thesis is: ***How does the coupled thermal-hydrological-mechanical response of rock salt around two adjacent boreholes control the migration of gas from one borehole to the other in the BATS II configuration, and to what extent can a coupled three-dimensional THM model reproduce the experimental observations at the WIPP site?***

2. Experimental Background

This section describes the Brine Availability Test in Salt (BATS) II experimental setup, the main observations from the gas tracer test, and the modelling targets. A detailed description of the field program is provided by Kuhlman et al. (2024b).

2.1. Experimental Setup

The BATS II experiment was conducted at the Waste Isolation Pilot Plant (WIPP) in bedded rock salt near Carlsbad, New Mexico, at a depth of approximately 655 m. The underground test array consists of a central heater borehole (HP) and parallel horizontal boreholes drilled from an operational drift (Fig. 2). The two boreholes used for the gas tracer test are the HP borehole (outlet) and the source borehole D (inlet), separated by a distance of approximately 20.3 cm in cross-section (Kuhlman et al., 2024b).

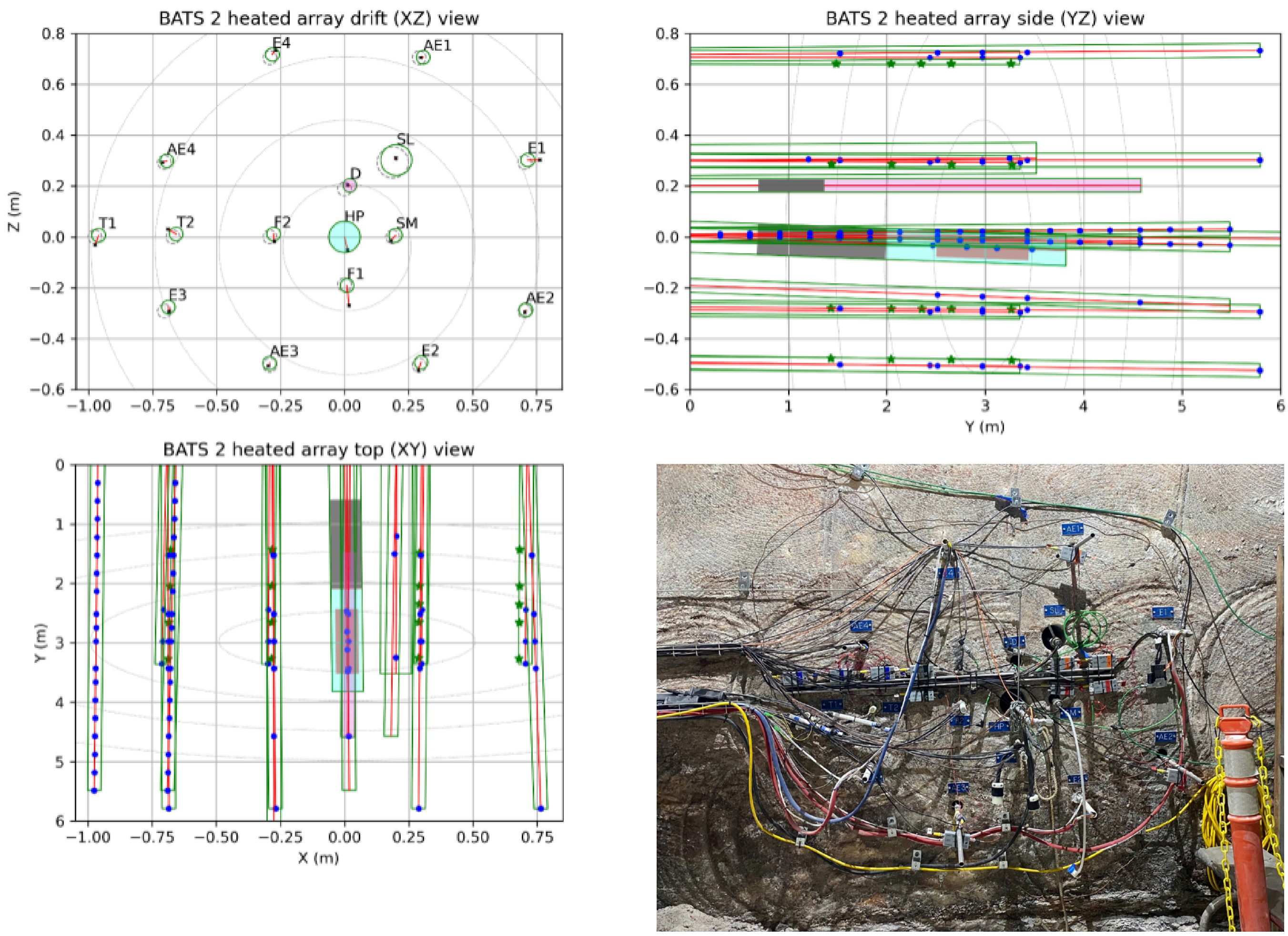

Figure 2. Drift, side, and top views of BATS 2 array. The drift view shows the proposed (gray dashed) and as-built (green) borehole positions in the drift; the red line is the borehole axis. The side and top views show thermocouple and resistance temperature detector (RTD) locations (blue dots), Acoustic emission (AE) sensor locations (green stars), HP heater (red box), and HP/D packers (gray boxes). The source interval is indicated in pink and the detector interval in cyan. Taken from Kuhlman et al., 2024b. The image on the bottom right shows the experimental setup at the WIPP facility.

The HP (outlet) borehole has a radius of 6.095 cm and a total accessible gas interval between 1.98 m and 3.82 m from the drift face, giving a 1.84 m long sink area for the argon to be in. Inside that borehole, a heating source (heater) was inserted, with a setpoint temperature of 140°C, as well as a mechanical packer that isolates the heated interval from the drift, and a series of thermocouples. Dry nitrogen is continuously circulated through the heated interval at a nominal flow rate of 100 standard mL/min (Kuhlman et al., 2024).

The D (inlet) borehole has a radius of 2.665 cm and an accessible gas interval between 1.53 m and 4.60 m depth, behind a mechanical packer. Argon is pressurized behind this packer to act as the gas source for the tracer test. Argon was selected for its chemical inertness and ideal-gas behaviour under WIPP conditions, ensuring it migrates only by advection without reacting with the host rock or brine. The gas stream exits the borehole and passes through a quadrupole mass spectrometer for compositional analysis, allowing the relative concentration of argon in the HP gas stream to be tracked over time (Kuhlman et al., 2024). Six temperature sensors (F1, F2, E2, T1a, T1b, T2) in adjacent boreholes (Appendix, Table A1), at known radial distances from the HP heater centreline, provide the thermal dataset used for the benchmark described in Section 5.1.1 (Kuhlman et al., 2024).

2.2. Gas tracer test observations

The BATS-2g gas tracer test has three distinct phases: a pre-heating argon breakthrough period, an eight-week heating period during which argon flow stopped, and a post-heating breakthrough period (Fig. 3). The key dates and times are listed in Table 1. On the 30^{th} of May 2024, the D borehole was pressurized to 20.3 psi (gauge; 241.29 kPa absolute) with argon; 7.63 standard litres of argon were added to fill the interval from near-ambient pressure. Over the following days, the D borehole pressure decayed as argon migrated toward HP, reaching approximately 9.71 psi (gauge; 168.27 kPa absolute) by June 3^{rd} 2024; this decay is the main calibration target for the fracture hydraulic parameters (Section 5.1.2). The D borehole was re-pressurized to 20.8 psi (gauge; 244.74 kPa absolute) on the morning of June 3^{rd} 2024, shortly before heating began. The heater power jumped immediately to approximately 1200 W, then rapidly stabilized to a steady-state value of approximately 600 W (Kuhlman et al., 2024b).

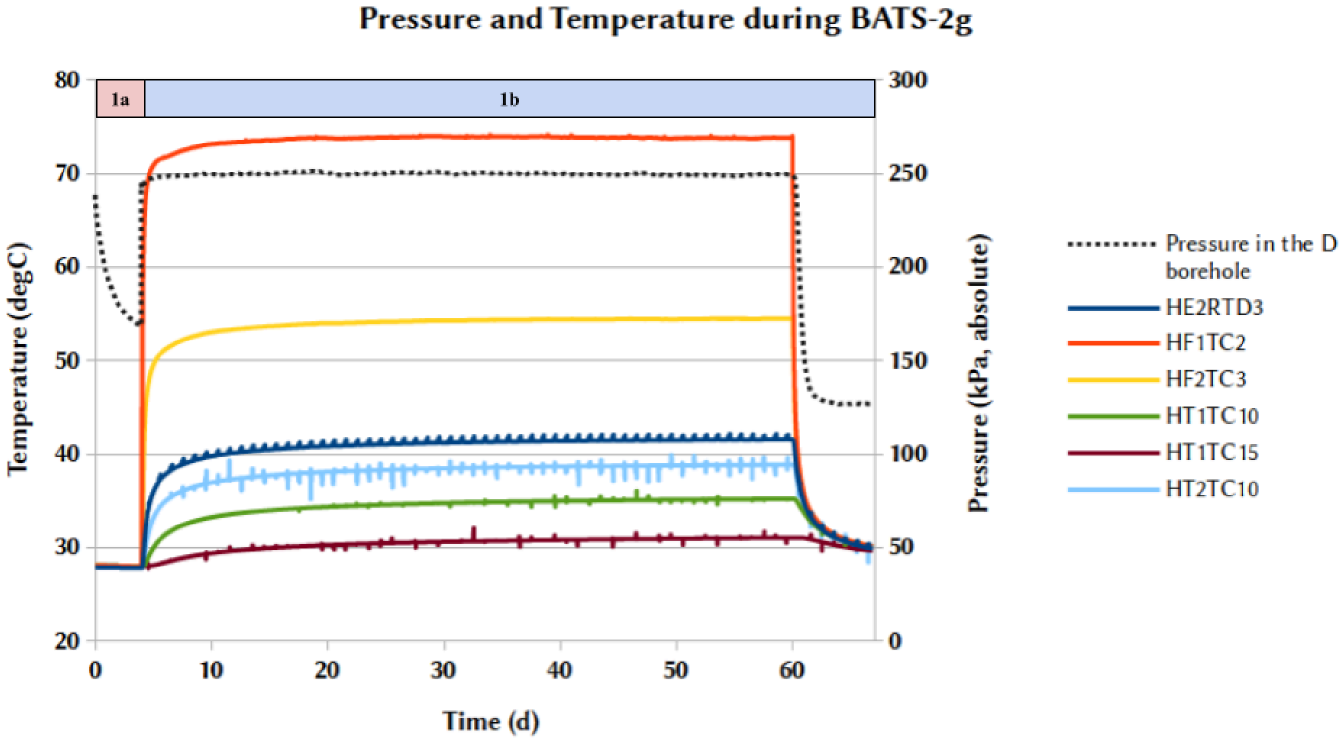

Figure 3. Pressure (in kPa, absolute) in the inlet (D) borehole and temperature (°C) measured at the different sensors (Appendix, Table 1A) over the course of the BATS-2g gas tracer test (late May to early August 2024). Step 1a is modelled under ambient conditions to show the migration of argon from one borehole to another, through a decrease in pressure in the D borehole. Step 1b is modelled over the remainder of the simulation, once heating starts and is subsequently stopped.

Within approximately 0.05 days (~70 minutes) of heating onset, the argon concentration in the HP gas stream declined significantly, indicating that gas migration had slowed down and then stopped. Argon flow remained undetectable throughout the eight-week heating period, which ended on July 29th 2024. Following the cessation of heating, argon breakthrough at HP resumed, peaking at midnight on the 30th of July 2024 (Fig. 3). The recovery of 7.23 standard litres of argon at HP following heating, compared to the 7.63 standard litres injected into D (a ratio of approximately 95%), showcases that most of the argon migrated through the salt along a preferential hydraulic pathway.

Table 1. Key dates and times for the BATS-2g gas tracer test (adapted from Kuhlman et al., 2024b).

Date / Time	Event
30^{th} of May 2024, 09:40 AM	D borehole pressurized to 20.3 psi gauge (241.29 kPa); 7.63 std L argon injected; t= 0 for Step 1a
3^{rd} of June 2024, 08:40-08:50 AM	D borehole re-pressurized to 20.8 psi gauge (244.74kPa)
3^{rd} of June 2024, 09:15 AM	Heating started (setpoint 140°C); t = 0 for Step 1b
3^{rd} of June 2024, ~10:30 AM	Argon flow at HP ceases (～70 minutes after heating onset)
29^{th} of July 2024, 09:34 AM	Heating stopped; 56 days of heating

2.3. Modelling objectives

Four experimental objectives are used to evaluate the model. These modelling targets are shared across all DECOVALEX-2027 BATS II participating teams, allowing for comparison of results despite differences in the modelling approaches adopted by each team.

(1) **D borehole pressure [kPa] over time.** The pressure decay in D from 239.9 kPa to approximately 168.2 kPa over four days before heating is the primary calibration target for the fracture hydraulic parameters k_0 (initial permeability) and Ap_0 (initial aperture).
(2) **Argon mass lost from the D borehole [g].** This goal is paired with target 4 to evaluate how much argon reaches the HP borehole.
(3) **Argon mass flow rate at HP [g/s] over time.** These flow data entering the HP borehole constrain changes in fracture conductance before and after the onset of heating. The model must reproduce the pre-heating flow, its cessation within ～70 minutes of heating onset, and its resumption after heating stops.
(4) **Cumulated argon mass at HP [g].** The model should approach the observed total of 7.23 standard litres (~13 g) recovered at HP during the post-heating breakthrough, consistent with the 95% recovery rate.

Ultimately, the primary objective of the coupled 3D THM model is to reproduce the thermally driven closure and post-heating reopening of the fracture pathway. The model focuses on evaluating whether thermal stress expansion can account for the observed hydraulic behaviour and on identifying which structural parameters - aperture of the fracture (Ap), roughness (R) of the fracture planes, and fracture length (L) - control the timing and amplitude of the hydraulic shutoff.

3. Conceptual model

3.1. THM coupling conceptualization, model simplifications and assumptions

The proposed mechanism for the cessation of argon flow during heating is a thermal-mechanical-hydraulic chain reaction: the heater raises the temperature of the surrounding rock salt; thermal expansion generates compressive strain at the fracture; this reduces the fracture aperture; the reduced aperture lowers the fracture permeability; and the resulting permeability drops too low to sustain argon flow against the pressure gradient. The following simplifying assumptions are applied to the domain:

(1) **Linear elasticity.** The rock salt is treated as a linearly elastic solid. On the short timescale of the rapid argon shutoff (～70 minutes), elastic deformation dominates over creep, which requires days to weeks to accumulate significant strain at WIPP temperatures and stresses (Krieg et al., 1984; Cristescu & Hunsche, 1998).

(2) **Single-phase ideal gas.** Argon is treated as the only fluid phase and as an ideal gas. At the pressures and temperatures of the experiment (P ～ 130-240 kPa, T ～ 300-400 K), argon deviates from ideal behaviour by less than 0.1% (Little, 1964). Analysis of the gas during the experiment supports this choice: gas remained comparatively humid during the first month of heating but became progressively drier over the second month. This suggests that the heated borehole had dried out significantly by the end of BATS-2g and that late-stage transport was likely single-phase (Kuhlman et al., 2024b).

(3) **Homogeneous and isotropic salt.** At the scale of the $(10m)^3$ model domain, the lithology is treated as pure halite. This isotropic assumption is consistent with previous contributions (Tounsi et al., 2023; Ottenheim, 2025).

(4) **Single planar fracture.** The near-complete tracer recovery (95%) indicates a well-connected, preferential hydraulic pathway between boreholes D and HP. In this model, this pathway is conceptualized as a single planar fracture connecting the two borehole walls, following the setup of Ottenheim (2025).

(5) **Negligible gravitational and in-situ stress fields:** The primary driver of mechanical fracture closure is the thermal stress gradient rather than the absolute baseline stress. A key characteristic of linear elasticity is that the transient thermal stress response does not depend on the system's pre-existing stress state (Boley & Weiner, 1960).

3.2. Two-study modelling approach

The model evaluates the system behaviour through two successive numerical studies that share an identical geometry, finite element mesh, and physics interfaces. Those two studies aim to complete the BATS-2g steps 1a and 1b (Section 1.3; Fig. 3), and will help meet the modelling targets previously described (Section 2.3).

Step 1a: Ambient conditions. The heater power is zero, and the fracture aperture and permeability are held constant at Ap_0 and k_0 respectively. This study simulates the pre-heating argon breakthrough observed between the 30^{th} of May and the 3^{rd} of June 2024 (Fig. 3), and is used to calibrate k_0 and Ap_0 against the experimental D borehole pressure decay and cumulated argon mass at HP. For this study, the D borehole is initialized at 20.3 psi gauge.

Step 1b: Heating with subsequent cooling. The heater is activated, applying the experimentally recorded power time series to the HP borehole wall, and the permeability-aperture coupling is active. Step 1b simulates the full heating period from the 3^{rd} of June to the 29^{th} of July 2024 (55.92 days) and the subsequent post-heating cooling period (Fig. 3). The D borehole is initialized at 20.8 psi gauge, reflecting the re-pressurization that took place on the morning of 3^{rd} of June 2024 immediately before heating onset.

One of the modelling objectives (Section 2.3, 1^{st} objective) is evaluated over a continuous sweep (a parametric study with several parameter cases in a single instance) to calibrate and constrain parameters. After that, Step 1b is evaluated for three targeted single-parameter variations, following that calibration (Section 5.1.2). The parameters used are the fracture roughness factor R, initial aperture Ap_0, and along-borehole fracture length L - parameters defined and discussed in Sections 4.2.3.3 and 5.1.2.

(1) Run A - Calibrated best fit. This is the parameter set that best reproduces the Step 1a pressure decay and is the basis for the shutoff analysis in Section 6.2.

(2) Run B - Effect of fracture length. This run uses the same parameters as run A, but varies fracture length. Keeping roughness and aperture fixed isolates the effect of fracture length alone on pressure decay and on the timing of the modelled shutoff and post-heating breakthrough.

(3) Run C - Effect of a larger initial aperture. This run uses a fixed roughness factor and initial fracture length, but changes the initial aperture to isolate its effect. It tests whether a more permeable fracture still experiences a thermally driven shutoff, and how the timing and completeness of the shutoff and breakthrough compare to run A.

4. Numerical Model

4.1. Geometry and Mesh

The computational domain is a 10 m * 10 m * 10 m rock salt cube (Fig. 4). The HP borehole is modelled as a horizontal cylinder of radius 6.095 cm, positioned so that its centreline matches the WIPP experimental geometry (Fig. 2). The D borehole is a second cylinder of radius 2.665 cm, with its centre separated from HP by 20.3 cm. Only the gas-accessible interval of each borehole is represented in the model geometry: the HP borehole spans 1.84 m (from 1.98 m to 3.82 m from the drift face), and the D borehole spans 3.07 m (from 1.53 m to 4.60 m), consistent with the packer-isolated intervals reported in Table A1 of the Appendix. The fracture connecting the two boreholes is represented as a 2D internal surface (an extruded ZX work-plane) within the salt domain, oriented horizontally between the borehole walls. Five thermocouple positions (F1, F2, E2, T1a, T1b, T2) are represented as point probes at their radial distances from the HP centreline (Appendix, Table A1).

The domain is discretized with an unstructured tetrahedral mesh, refined near the HP borehole wall, the D borehole wall, and the fracture surface, where thermal and pressure gradients are steepest. Element size was controlled through five geometric entity levels using COMSOL's free tetrahedral mesh feature, with a scale factor of 1 everywhere unless otherwise specified. A coarse element size was applied to the bulk of the domain. A fine element size was applied to the boundaries of the fracture and of the two borehole walls, where the steepest thermal and pressure gradients occur. A finer element size was applied within a rectangular refinement zone around both boreholes (0.4 m wide * 3.2 m deep * 0.25 m high, centred at X = -0.12 m, Y = 1.5 m, Z = -0.13 m in the model coordinate system), enhancing local resolution around the heated interval without refining the entire domain (Fig. 4). A finer element size was also applied at each of the six thermocouple sensor points, to ensure accurate point-probe sampling. Finally, all remaining geometric entities were attributed the default free tetrahedral settings. The resulting mesh contains 29,769 mesh vertices, 175,596 tetrahedral elements, and 16,004 boundary triangular elements.

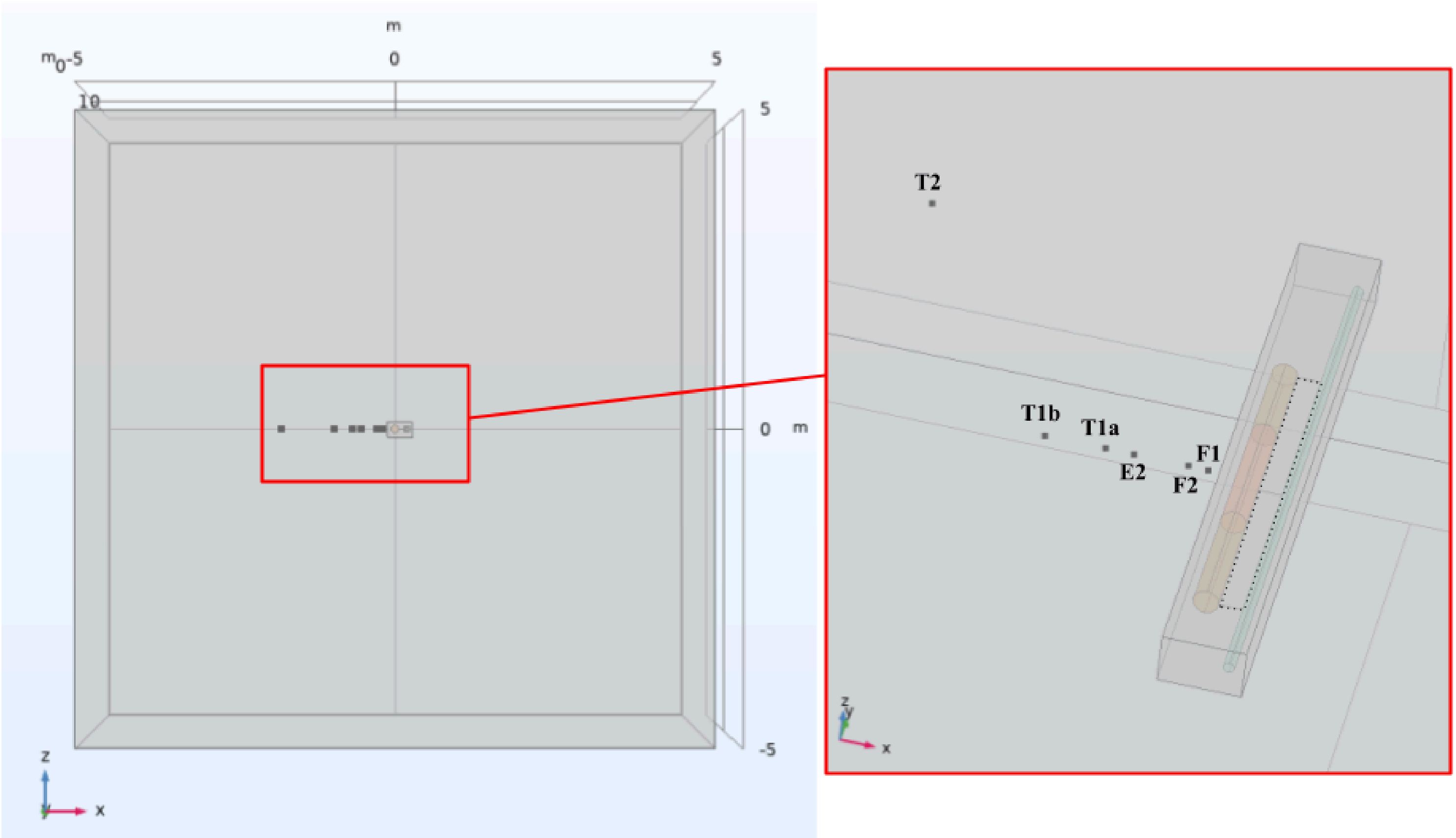

Figure 4. Geometry of the 3D coupled model domain (10 m × 10 m × 10 m rock salt cube; left), with a zoomed inset (right) showing the HP borehole (orange cylinder), heater (red cylinder) and D borehole (blue cylinder) arrangement and the spatial positions of the six thermocouple sensors (T2, T1b, T1a, E2, F1, F2) relative to the borehole array. The dotted black lines delineate the fracture; here it is 1.84 m long. For the 0.711m long fracture scenario, the fracture is centred at the same Y as the heater's center.

4.2. Material properties and governing equations

To reproduce the thermal field of the experiment, the argon flow between boreholes, and the thermally driven closure of the fracture, three coupled physics interfaces are implemented in COMSOL Multiphysics: thermal, hydrological, and mechanical components, whose governing equations are described in the following section.

4.2.1. Thermal component - Heat Transfer in Solids

4.1.1.1. Governing Equations

Heat transport in the thermal model is governed by the general transient conductive heat-transfer equation solved by the COMSOL Multiphysics Heat Transfer in Solids module:

$$\rho C_p(T)\frac{\partial T}{\partial t} = \nabla * (k(T)\nabla T)$$

where ρ is the density of the rock salt $[kg/m^3]$, $C_p(T)$ is the temperature-dependent specific heat capacity $[J/(kg * K)]$, $k(T)$ is the temperature-dependent thermal conductivity $[W/(m * K)]$, and T is the temperature [K]. The host rock is treated as a stationary solid, so the advective term is zero. No distributed heat sources are present within the rock salt domain; all thermal input enters the model exclusively through the heater boundary. The temperature-dependent functions $C_p(T)$ and $k(T)$ are derived from laboratory measurements on WIPP rock-salt core samples from the BATS-1 experiment (Kuhlman et al., 2020), as reported in Ottenheim (2025). The fitted expressions for the core sample used, and all other rock salt material properties used in the model, are listed in Table 2.

The heater is represented as a boundary surface heat flux applied to the heater's wall:

$$- n * q = Q_b, \; with \; Q_b = P_b/A$$

where P_b is the prescribed heater power [W] and A is the area of the heater surface $[m^2]$. The initial temperature throughout the domain is set to the ambient WIPP temperature at the start of the experiment (Kuhlman et al., 2024b):

$$T(x, 0) = T_0 = 28°\text{C} \; (301.15 \text{ K})$$

This same governing equation, initial condition, surface-flux representation of the heater, and temperature-dependent material properties are applied in both Ottenheim's 2D axisymmetric thermal model (2025) and this 3D thermal model; the two formulations therefore differ only in the geometry of the spatial domain.

Table 2: Rock salt material properties used in the thermal and mechanical components of the coupled model, including Young's modulus, Poisson's ratio, density, thermal expansion coefficient, temperature-dependent thermal conductivity and specific heat capacity, and matrix porosity and permeability. Young's modulus E = 30 GPa and Poisson's ratio v = 0.3 fall within the reported range for WIPP Salado Formation salt (Krieg et al., 1984). Matrix porosity and permeability are simplifications: intact Salado salt shows porosity averaging 0.4% (Physical Properties of WIPP Salt, 1981) and permeabilities of 10^{-21} *to* $10^{-20} m^2$ *(Sandia National Laboratories, 1988), with brine*

residing only in unconnected pores absent the EDZ (National Research Council, 1996); the fracture-dominated hydraulic connection between boreholes justifies the zero matrix permeability assumption.

Parameter	Symbol	Value	Unit	Source
Young's modulus	E	30	GPa	Bruno (2002), Krieg et al. (1984)
Poisson's ratio	υ	0.3	-	Bruno (2002), Krieg et al. (1984)
Density	ρ	2300	kg/m^3	LaForce et al. (2022)
Thermal expansion coefficient	α	$4.0 * 10^{-5}$	K^{-1}	Kuhlman et al. (2024b)
Thermal conductivity	$k(T)$	H-HP_2.5: −4.11 ln(T) + 28.142	W/(m*K)	Kuhlman et al. (2024b); Ottenheim (2025)
Specific heat capacity	$C_p(T)$	H-HP_2.5: $-0.0045T^2$ + 3.9286T + 0.722	J/(kg*K)	Kuhlman et al. (2024b); Ottenheim (2025)
Matrix porosity	ε	10^{-7}	-	Model assumption
Matrix permeability	κ	0	m^2	Model assumption

4.2.2. Hydrological component - Darcy's Law

4.2.2.1. Governing Equations

Gas transport through the porous rock salt is modelled using the COMSOL Multiphysics Darcy's Law interface. The Darcy velocity u [m/s], representing the volumetric flow rate of fluid per unit cross-sectional area of the porous medium, is related to the pressure gradient by Darcy's law:

$$u = -(\kappa/\mu)\nabla P$$

where κ is the permeability [m^2], μ is the dynamic viscosity of the fluid [Pa/s], and P is the fluid pressure [Pa]. Combining Darcy's law with the continuity equation yields the pressure-evolution equation integrated in time:

$$S_p \frac{\partial P}{\partial t} + \nabla * (u) = 0$$

where S_p is the storage coefficient [Pa^{-1}]. No distributed fluid sources are present within the rock salt ($Q_m = 0$); argon enters and leaves the domain exclusively through the inlet and outlet boreholes. The storage coefficient S_p is not specified as an input. Instead, COMSOL's "Density and porosity" storage model is selected, and S_p is computed internally in each domain from the density and porosity of the materials assigned to that domain:

$$S_p = \varepsilon\chi_f + (1 - \varepsilon)\chi_p$$

where ε is the porosity, χ_f is the isothermal compressibility of the fluid [Pa^{-1}], and χ_p is the effective compressibility of the solid matrix [Pa^{-1}]. This domain-dependent formulation is physically more consistent than the single fitted S_p value of $10^{-6.73} Pa^{-1}$ used by Ottenheim (2025) and automatically ensures that storage behaviour reflects the properties of each subdomain. Argon is treated as an ideal gas; its fluid properties are listed in Table 3.

Table 3: Argon fluid properties used in the hydrological model, including molar mass, dynamic viscosity, density (via the ideal gas law), and the universal gas constant.

Parameter	**Symbol**	**Value**	**Unit**	**Source**
Molar mass	M	0.03995	kg/mol	(Chase, 1998)
Dynamic viscosity	μ	2.22×10^{-5}	Pa·s	Evaluated at 28°C, ~100 kPa

Density	ρ	$PM/(RT)$	kg/m³	Ideal gas law
Gas constant	R	8.314	J/(mol·K)	(Chase, 1998)

Table 4: Porosity and permeability assigned to each domain in the hydrological model (rock salt matrix, HP borehole, D borehole), reflecting the hydraulically inactive matrix and the effective open-cavity behaviour of each borehole. The boreholes are represented as open gas cavities rather than porous media - permeability is assigned as sufficiently high to ensure instantaneous pressure equilibrium within each borehole relative to the much slower timescale of fracture-controlled gas migration. In COMSOL's Darcy Law interface, a porous domain with such elevated permeability behaves hydraulically as a free-flowing volume.

Domain	Porosity ε	Permeability κ (m²)	Notes
Rock salt matrix	10^{-7}	0	Hydraulically inactive
HP borehole	0.7	10^{-8}	Effective porosity; accounts for heater, packer, instrumentation.
D borehole	1.0	10^{-8}	/

4.2.2.2. Fracture Representation

To reproduce the preferential gas flow observed in the experiment, a fracture is included in the hydrological model using the Fracture Flow feature of COMSOL's Darcy's Law interface - a 2D internal surface. The gas recovery rate supports this choice during the experiment (～95%). This rate is incompatible with diffusion through an intact salt matrix, whose permeability is on the order of $10^{-21} m^2$ (Krieg et al., 1984). It supports the presence of a discrete preferential flow path. The fracture aperture Ap [m] is not resolved as a geometric thickness in the mesh but as a parameter of the fracture-flow equations.

Within the fracture, COMSOL integrates the tangential mass balance:

$$Ap \frac{\partial(\varepsilon_p)}{\partial t} + \nabla_T * (Ap * \rho u) = 0$$

and Darcy's law with the tangential pressure gradient:

$$u = -\left(\frac{\kappa_f}{\mu}\right)\nabla_T P$$

where Ap is the fracture aperture [m], ε_p is the fracture porosity, κ_f is the fracture permeability [m^2], and ∇_T is the tangential gradient operator, restricting spatial derivatives to the plane of the fracture. The pressure inside the fracture is coupled to the pressure in the adjacent rock-salt domains through pressure and mass-flux continuity at the fracture-rock interface. The fracture permeability κ_f is determined from the fracture aperture using the cubic law with a roughness correction, as described in Section 4.2.3.3. In the first study step (step 1a), the aperture is held constant at its calibrated value Ap_0; in the second one (step 1b), the aperture evolves in response to the thermally induced mechanical deformation, as described in Section 4.2.3. The borehole domain properties - porosity and permeability assigned to each domain in the hydrological model - are listed in Table 4.

4.2.3. Mechanical Component - Solid Mechanics

4.2.3.1. Governing Equations

The mechanical behaviour of the rock salt matrix is modelled within a quasistatic solid. Indeed, because the rates of thermal expansion and hydraulic pressurization are small relative to elastic wave propagation velocities (Boley & Weiner, 1960), inertial terms are omitted from the momentum balance:

$$0 = \nabla \cdot S + f_V$$

where S is the Cauchy stress tensor [Pa] and f_V is the body force per unit volume [N/m^3], here set to 0 ($f_V = 0$) in the rock salt domain. The stress tensor is decomposed into elastic and inelastic contributions:

$$S = S_{el} + S_{inel}, \qquad S_{inel} = S_0 + S_{ext} + S_q$$

with the corresponding strain decomposition:

$$\varepsilon_{el} = \varepsilon - \varepsilon_{inel}, \qquad \varepsilon_{inel} = \varepsilon_0 + \varepsilon_{ext} + \varepsilon_{th} + \varepsilon_{hs} + \varepsilon_{pl} + \varepsilon_{ic} + \varepsilon_{cr} + \varepsilon_{vp} + \varepsilon_{ve}$$

where the inelastic strain contributions are, in turn, initial strain ε_0, externally imposed strain ε_{ext}, thermal strain ε_{th}, hygroscopic swelling ε_{hs}, initial creep ε_{ic}, plastic strain ε_{pl}, creep strain ε_{cr}, viscoplastic strain ε_{vp} and viscoelastic strain ε_{ve}. In the present mechanical model, none of these inelastic strain mechanisms is active in the bulk rock salt: the surrounding rock salt is treated as a purely linear-elastic material, so $\varepsilon_{inel} = 0$ and the total strain reduces to its elastic part throughout the bulk domain. The fracture is treated separately using the thin-layer spring formulation of Section 4.2.3.2.

Total strain (ε) is related to the displacement field u via the standard kinematic relation:

$$\varepsilon = \frac{1}{2}\left[(\nabla u)^T + \nabla u\right]$$

and the elastic constitutive relation is:

$$S_{el} = C : \varepsilon_{el}, \qquad C = C(E, v)$$

where C is the fourth-order elasticity tensor, determined by the Young's modulus E and the Poisson's ratio ν of the material (Table 2).

4.2.3.2. Thin Elastic Layer - Fracture

In this physics node, the fracture is represented mechanically as a thin elastic layer using the Thin Layer feature of COMSOL's Solid Mechanics interface, with a non-layered elastic spring approximation. The fracture is collapsed onto a 2D internal surface in the 3D coupled model. The two faces of the fracture are linked by a distributed spring whose traction per unit area opposes their relative displacement.

$$f_A = -\, k_A\, u_e$$

where f_A is the spring traction vector $[N/m^2]$, k_A is the isotropic spring stiffness (Table 3; Appendix, Fig. A11; [Pa/m]), and $u_e = u_u - u_d$ represents the relative displacement vector between the upper (u) and lower (d) fracture faces. The normal component of u_e determines how the fracture aperture evolves.

4.2.3.3. Permeability-Aperture coupling

In the coupled 3D model (Step 1b), the fracture permeability κ_f is updated at each timestep from the current aperture Ap using the cubic law with roughness correction (Witherspoon et al., 1980):

$$\kappa_f = Ap^2/(12R)$$

where R is the dimensionless roughness factor that accounts for the deviation of the real fracture from the idealized smooth parallel-plate geometry. For smooth parallel plates $R = 1$, recovering the classical cubic law; for rough fractures $R > 1$, reducing the effective permeability for a given aperture.

In Step 1a, $Ap = Ap_0$ is constant and $\kappa_f = \kappa_0 = Ap_0^2/(12R)$. In Step 1b, as thermal expansion compresses the fracture, Ap decreases, and κ_f decreases with the square of the aperture.

4.3. Boundary and initial conditions

All numerical models were implemented in COMSOL Multiphysics 6.4. The fully coupled 3D THM model activates three physics interfaces simultaneously: Heat Transfer in Solids (Section 4.2.1), Darcy's Law with Fracture Flow (Section 4.2.2), and Solid Mechanics with Thin Layer (Section 4.2.3). The Thermal Expansion Multiphysics node links the thermal and mechanical interfaces. All three interfaces share the same mesh and are solved fully coupled at each timestep using a direct solver.

The boundary and initial conditions for the thermal model are described in Section 4.3. The initial temperature is set to T_0 = 28°C (301.15 K) throughout the domain. The drift-facing boundary is assigned a time-varying temperature with a seasonal drift, to account for the seasonal temperature changes, with a maximum ambient temperature variation of 2 °C between summer and winter (Ottenheim, 2025). All remaining outer boundaries are thermally insulating ($\partial T/\partial n = 0$).

For the hydrological component of the model, the D borehole is assigned a specific prescribed initial pressure boundary condition to reproduce the experimental conditions (Table 5). The HP borehole is assigned an initial pressure of 3.4 psi gauge (124.77 kPa absolute). This value was taken from the baseline reported in the BATS experimental data, consistent with the post-heating observation that the D borehole pressure equilibrates at approximately 3.66 psi gauge, supporting 3.4 psi gauge as a reasonable ambient pressure for the HP borehole interval. The fracture's flow model is Darcian; its storage model is based on density and porosity; and its model is a highly conductive fracture. No-flow conditions are applied to all outer boundaries of the salt.

For the mechanical component of the model, all outer boundaries are fixed in the normal direction (roller boundary conditions). The boreholes and fracture were given prescribed displacements of 0 and free in the X, Y, and Z directions, respectively. The initial mechanical stress is zero throughout the domain. All boundary and initial conditions are summarised in Table 5.

Table 5: Boundary and initial conditions for Step 1a and 1b.

Condition	Step 1a	Step 1b	Unit
D borehole pressure	20.3 (241.29 kPa absolute)	20.8 (244.74 kPa absolute)	psi gauge
HP borehole pressure	3.4 (124.77 kPa absolute)	3.4 (124.77 kPa absolute)	psi gauge
Heater power P_b	0 W	~600 W (BATS experimental data, time-varying)	W
Permeability-aperture coupling	Inactive	Active	-
Initial temperature T_0	28°C (301.15 K)	28°C (301.15 K)	K
Initial mechanical stress	0	0	Pa

4.4. Solver Setting

The time-dependent solver uses the Backward Differentiation Formula (BDF) method with adaptive timestepping. The initial timestep is set to 10^{-4} days to resolve the pressure and temperature gradients immediately after heating begins. The maximum timestep is 0.001 days during the first 0.5 days of Step 1b, increasing to 0.5 days thereafter. A relative tolerance of 10^{-2} and an absolute tolerance of 10^{-3} are applied. Within each timestep, the nonlinear system is resolved using a segregated solver approach, splitting the solution into pressure, temperature and mechanics variable groups rather than solving all variables simultaneously. This segregated method uses tolerance-based termination, with a maximum of 10 iterations per timestep and a tolerance factor of 1. Convergence is sped up using Anderson acceleration, with an iteration space dimension of 5, a mixing parameter of 0.9, and an iteration delay of 1. The Anderson step threshold is set to 10. Each variable group is solved using an algebraic multigrid (AMG) preconditioner with a direct solver. Constraint consistency is enforced strictly during the initial iteration.

5. Results

5.1. Parameter calibration

5.1.1. Thermal Benchmark: 3D vs. 2D axisymmetric

To ensure consistency and validate the 3D thermal component of the model before proceeding to the fully coupled analysis, the results were compared against the 2D axisymmetric model results developed by Ottenheim (2025) (Appendix, Fig. A1). Both configurations were run with identical material properties and boundary conditions to compare temperature evolution at six spatial sensor locations.

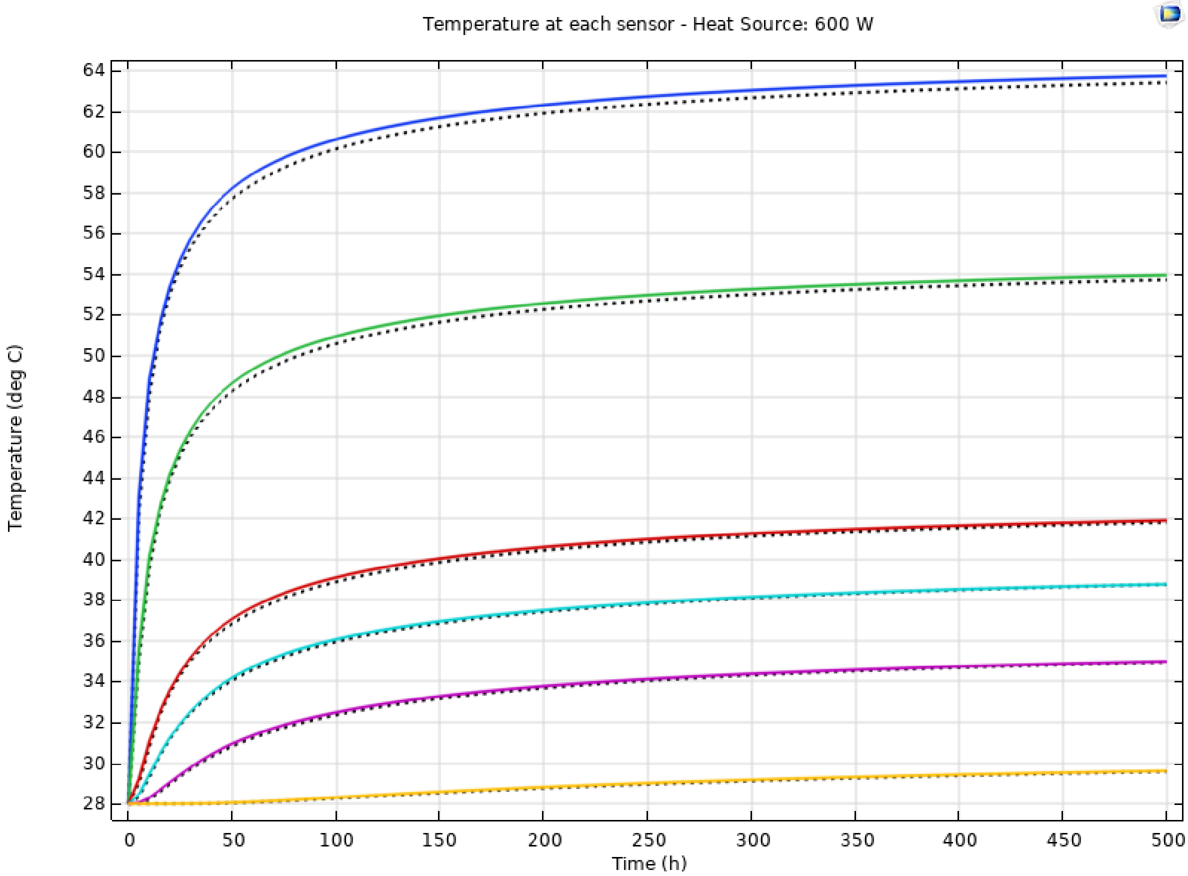

Figure 5. Temperature evolution at each of the six sensor positions for the 3D (dotted) and 2D axisymmetric (continuous) thermal models, with a heater power of 600 W (93% efficiency). Close agreement between the two geometries across all sensor locations confirms that the 3D thermal implementation reproduces the established 2D axisymmetric reference solution from Ottenheim's model (2025).

The results for the 600 W run are shown in Figure 5. This value is not arbitrary: 600 W corresponds approximately to the steady-state heater power recorded experimentally once the temperature controller stabilized the heater at its 140°C setpoint (Section 2.2). This power level also approximately reflects the thermal state once the fracture has closed and the argon flow has stopped. As in the coupled 3D model, a heater efficiency of 93% was applied to this run.

The point probes in the 3D model have the same radial distances from the HP borehole centerline as the corresponding nodes in the 2D reference mesh (Appendix, Table A1). However, minor variations are attributable to spatial discretization and mesh refinement disparities between the two dimensions. Figure A16 in the Appendix shows the effects of varying the mesh size, with a finer mesh allowing the model data to better match the experimental data.

5.1.2. Step 1a: Hydraulic calibration under ambient conditions

The fracture hydraulic parameters (initial aperture Ap_0, roughness factor R, and along-borehole fracture length L) were calibrated against the D borehole pressure decay observed between the 30^{th} of May and the 3^{rd} of June 2024 (Step 1a). The reference permeability k_0 is not an independent parameter but is derived from the calibrated Ap_0 and R via the cubic law (Section 4.2.3.3).

Calibration proceeded in two stages. In the first, R was varied over 1, 5, and 10; the fracture length over 0.711, 1.2, and 1.84 m; and aperture over $1 * 10^{-8}$, $1 * 10^{-7}$, and $1 * 10^{-5}$m. The results (as shown in the Appendix, Fig. A2) showed that all combinations with apertures of $1 * 10^{-6}$ m produce pressure decays that are too fast, reaching equilibrium within approximately 70 minutes regardless of R or fracture length. On the other hand, apertures of $1 * 10^{-8}$ m produce essentially flat curves that barely decay over four days. None of the R = 1 combinations reproduce the experimental curve, confirming that the smooth parallel-plate cubic law is insufficient. The closest matches for that stage are obtained with R = 5-10 and apertures around $1 * 10^{-7}$ m.

In the second stage, R was varied over 1, 3, 8, and 10, and aperture over $1 * 10^{-5}$, $5 * 10^{-6}$, $1 * 10^{-6}$, and $1 * 10^{-7}$ m, with fracture length fixed at 0.711 m. The refined sweep reveals a parameter trade-off (Appendix, Fig. A3): increasing R while simultaneously increasing the aperture can produce nearly identical pressure decay curves, because both combinations yield a similar k_0. The best-fitting combinations for this stage are in the R = 3-8 range with apertures between $1 * 10^{-6}$ and $5 * 10^{-6}$ m.

Based on the optimization results, the parameter set containing R = 3.5, Ap_0 = $3.1 * 10^{-6}$ m, L = 0.711 m was selected as the calibrated baseline (Appendix, Fig. A13). This configuration yields a reference fracture permeability of $k_0 \sim 2.3 * 10^{-13} m^2$, resulting in a pressure decay curve that closely matches the experimental data throughout the 4-day pre-heating period (Fig. 6).

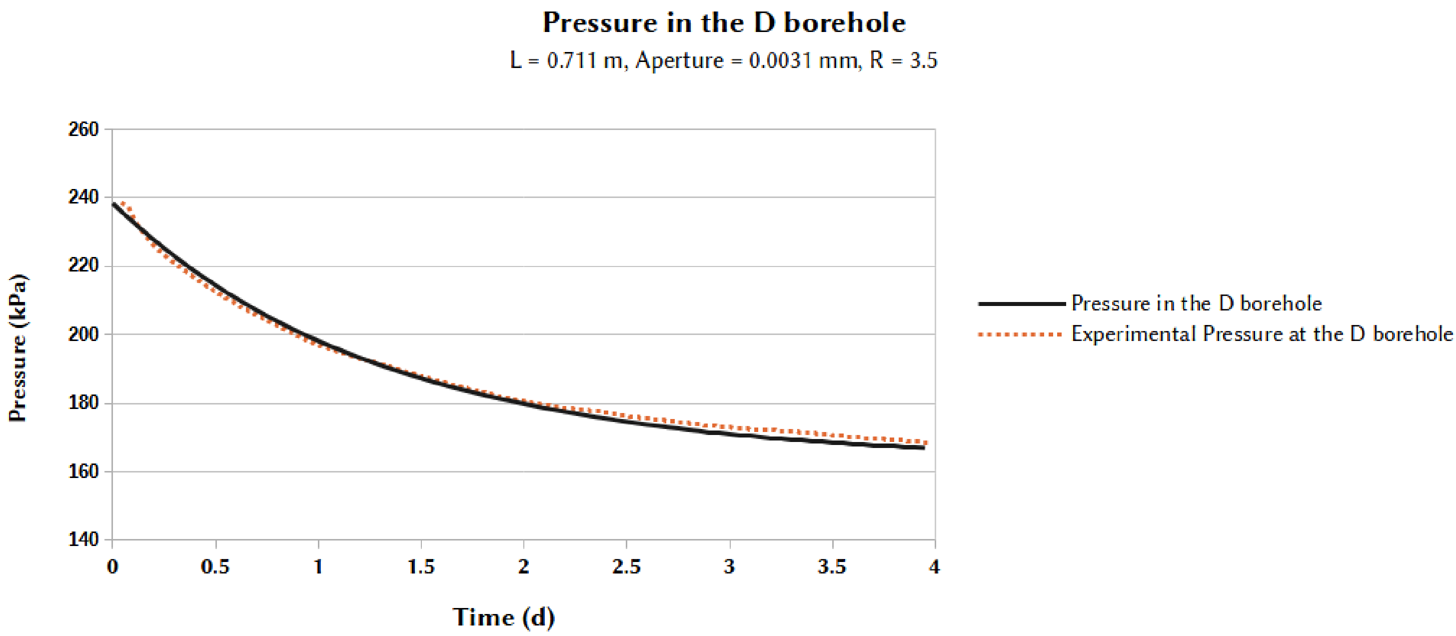

Figure 6. D borehole pressure versus time during Step 1a, for the calibrated best-fit parameter set (L = 0.711 m, Ap_0 = 0.0031 mm, R = 3.5), compared against the experimental pressure decay over the full 4-day pre-heating window.

5.2. Modelling Step 1a: Gas migration between the two boreholes

5.2.1. Objectives 1 and 2: Pressure decay in the D borehole and mass of Argon leaving the D borehole

The parameter sweep presented in this section was carried out as part of the calibration process described in Section 5.1.2, in which the experimental pre-heating pressure decay was used to identify the fracture parameters that best reproduce the observed flow between D and HP. Step 1a focuses on the unheated, pre-heating decay of D borehole pressure as argon migrates toward HP through the calibrated fracture, and identifies the roughness factor R that best reproduces the experimental decay among the values tested (R = 1, 3.5, and 8), at the calibrated aperture (Ap_0 = 0.0031 mm) and at both fracture lengths (L = 0.711 m and L = 1.84 m).

Figure 7a shows the modelled D borehole pressure for six R-L combinations against the experimental record. The complete sweep can be found in the Appendix (Fig. A4 & A5), along with an error analysis showing the difference between model data and experimental data (Fig. A13). All cases start from the same initial pressure of approximately 238 kPa (absolute) and decay as argon migrates from D to HP through the fracture. The decay rate increases with decreasing R, consistent with the inverse dependence of fracture permeability on roughness in the cubic law (Section 4.2.3.3): R = 1 (Fig. 7; red lines) decays fastest and plateaus earliest, reaching its equilibrium pressure of approximately 163 kPa within about one day; R = 8 (Fig. 7; green lines) decays more slowly and has still not approached equilibrium by the end of the model run, remaining above 180 kPa; and R = 3.5 (Fig. 7; blue lines) decays at an intermediate rate that closely matches the experimental curve throughout, staying within a few kPa of the measured pressure at every time step shown. Increasing the fracture length from 0.711 m to 1.84 m speeds up the decay for a given R, since a longer fracture has a larger cross-sectional area and therefore greater conductance (Section 5.1.2); for each R value, the L = 1.84 m case reaches the same plateau as its L = 0.711 m counterpart, but does so faster.

Figure 7b shows the corresponding mass of argon removed from the D borehole by the end of Step 1a. The experimental value is approximately 7.58 g, determined from the experimental pressure data. At L = 0.711 m, R = 1 overshoots this value (～8.24 g; continuous red line), R = 3.5 matches it most closely (～7.79 g; continuous blue line), and R = 8 undershoots it (～5.96 g; continuous green line). R = 3.5 therefore provides the best match to both the decay shape and the cumulative mass transferred, and is defined as the calibrated roughness factor in Section 5.1.2, constrained by the R = 1 and R = 8 cases on either side.

An important feature of Figures 7a & b is that, for R = 1 and 3.5, the L = 0.711 m (continuous red line) and L = 1.84 m (dashed red line) cases remove almost the same mass of argon (～8.247g and 7.798 g, respectively, for R = 1 and 3.5), despite reaching that point at different rates. Indeed, the total mass exchanged between D and HP at equilibrium is set by a mass balance over the compressible gas storage of each borehole and the initial pressure difference between them; and the parameters tested dictate only the rate at which equilibrium is approached. Once both fracture lengths have almost or fully equilibrated, by the end of the

Step 1a window, their final removed masses converge, even though the L = 1.84 m case reaches that state much faster.

(a)

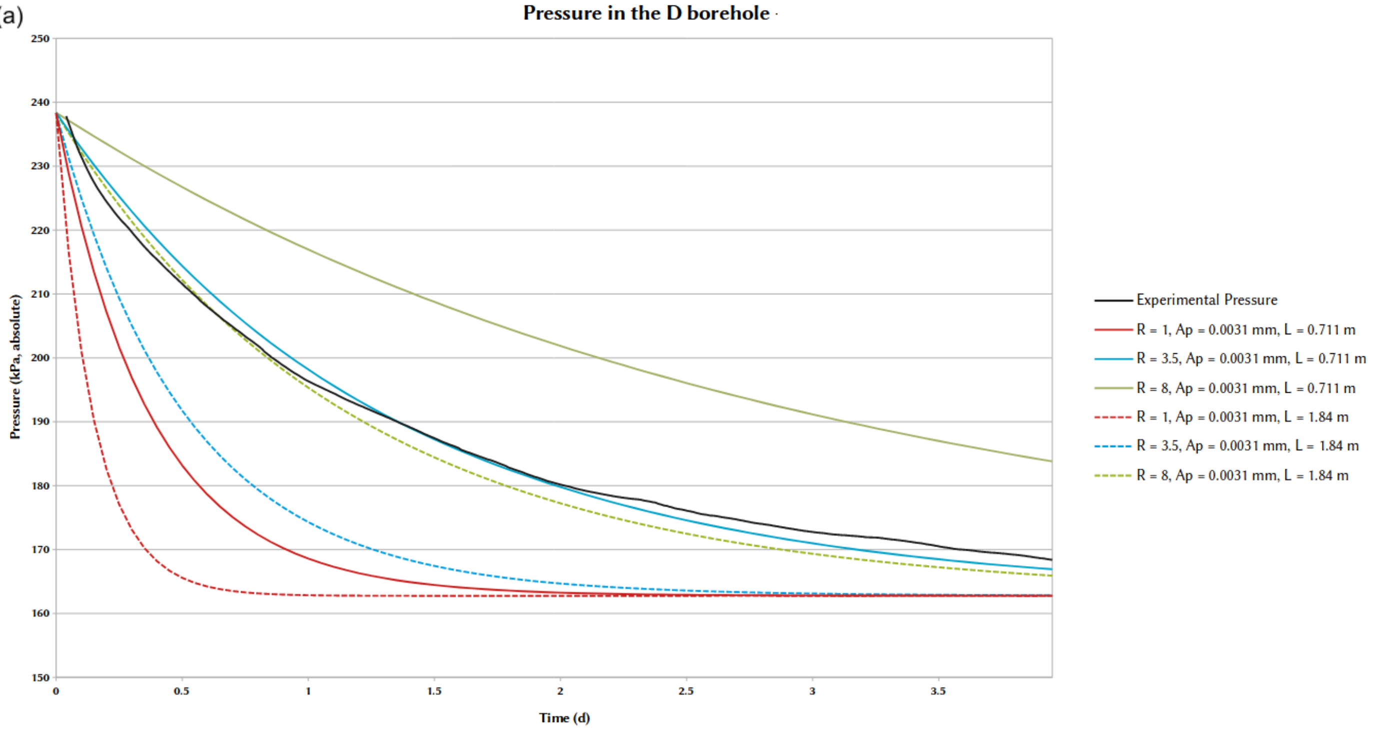

(b)

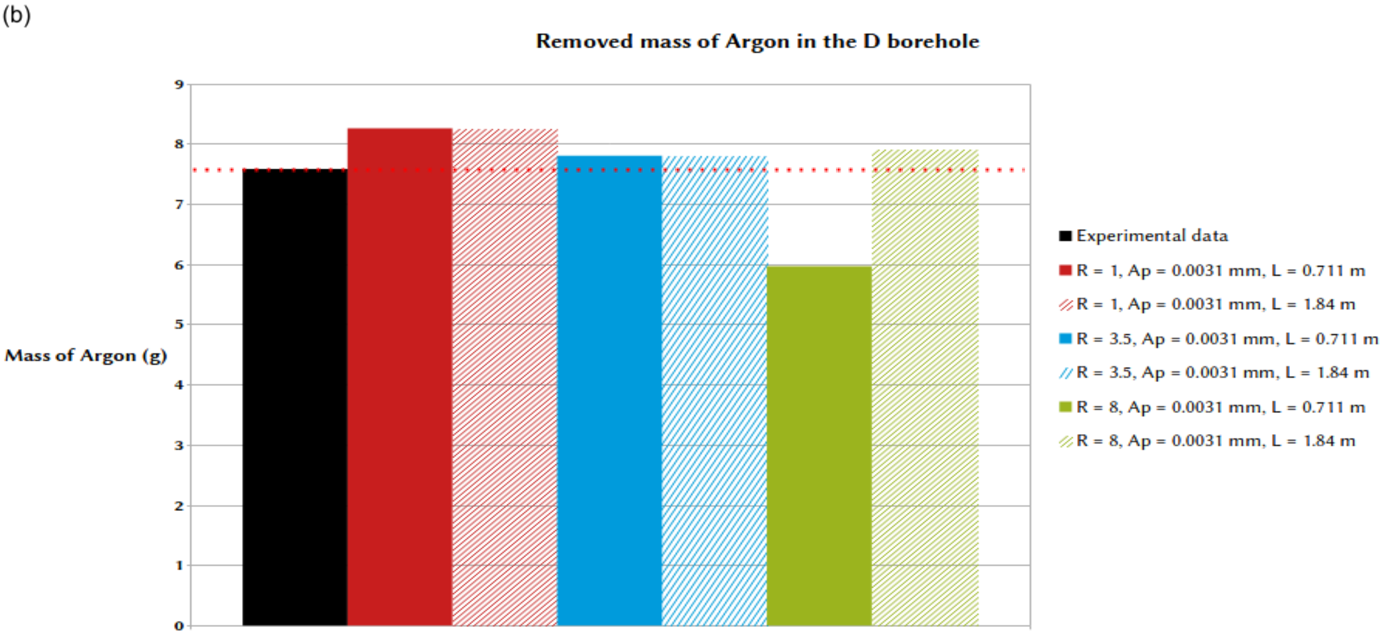

Figure 7. (a) D borehole pressure decay during Step 1a for the calibration sweep at fixed aperture (0.0031 mm), across R = 1 (red), 3.5 (blue), and 8 (green) and fracture lengths L = 0.711 m (continuous) and 1.84 m (dashed), compared against the experimental pressure record. (b) Corresponding cumulative argon mass removed from the D borehole at the end of Step 1a for each

combination. R = 3.5 provides the closest match to both the pressure decay shape and the cumulative mass transferred, supporting its selection as the calibrated roughness factor (Section 5.1.2). The dotted red line corresponds to the experimental value.

5.2.2. Objectives 3 and 4: Argon mass flow rate and cumulated argon mass at the HP borehole

The results in this section and onwards use the terms "run A, B and C". The purpose of each run is described in section 3.2. Run A uses the following set of parameters: R = 3.5, $Ap_0 = 3.1 * 10^{-6}$ m, L = 0.711 m; run B: R = 3.5, $Ap_0 = 3.1 * 10^{-6}$ m and run C: R = 3.5, $Ap_0 = 1 * 10^{-4}$ m (0.1 mm). Any reference thereafter to those runs therefore represents the sets just defined. In figures, run A is depicted with a blue continuous line, run B with a dashed blue line and run C with a green continuous line (unless stated otherwise).

Figure 8a presents the cumulative mass of argon entering the HP borehole over the four-day pre-heating window for runs A, B, and C, alongside the experimental cumulative mass derived from the quadrupole mass spectrometer data. Run B has the highest cumulative mass (8.24 g), consistent with its accelerated pressure decay (Fig. 8a and Fig. 8b): the longer fracture has a larger cross-sectional area for flow, driving the system toward equilibrium quicker. Run C yields 7.61 g - slightly below run A (7.77g) despite its larger aperture, which reflects the competing effect of fracture storage: while a larger aperture increases conductance, it also provides greater storage within the fracture itself, which ultimately delays HP pressure buildup. All three modelled values exceed the experimental total of approximately 7.58 g. This is consistent with the results in Figure 7, as more gas was computed leaving the D borehole than the experiment recorded.

Figure 8b shows the corresponding mass flow rates, derived from the time derivative of the cumulative pressure-based mass. A magnified view of the early simulation (t = 0 to 0.5 days) period is provided in the Appendix (Fig. A14). The experimental curve exhibits a peak of approximately $9 * 10^{-5} g/s$ (black continuous line) at around t ∼ 0.15 days. All three runs modelled have curves that peak earlier (within 0.05-0.1 days) and at different magnitudes. Run A (blue continuous line) reaches $7.59 * 10^{-5} g/s$, run B (blue dashed line) $5.53 * 10^{-4} g/s$ and run C (green continuous line) $1.76 * 10^{-3} g/s$, before decaying to near-zero values. Run A's peak magnitude is close to the experimental peak; however, it happens earlier. Runs B and C exhibit higher peaks, reflecting their larger fracture conductance and storage, thereby driving faster initial HP pressurization (Appendix, Fig. A14).

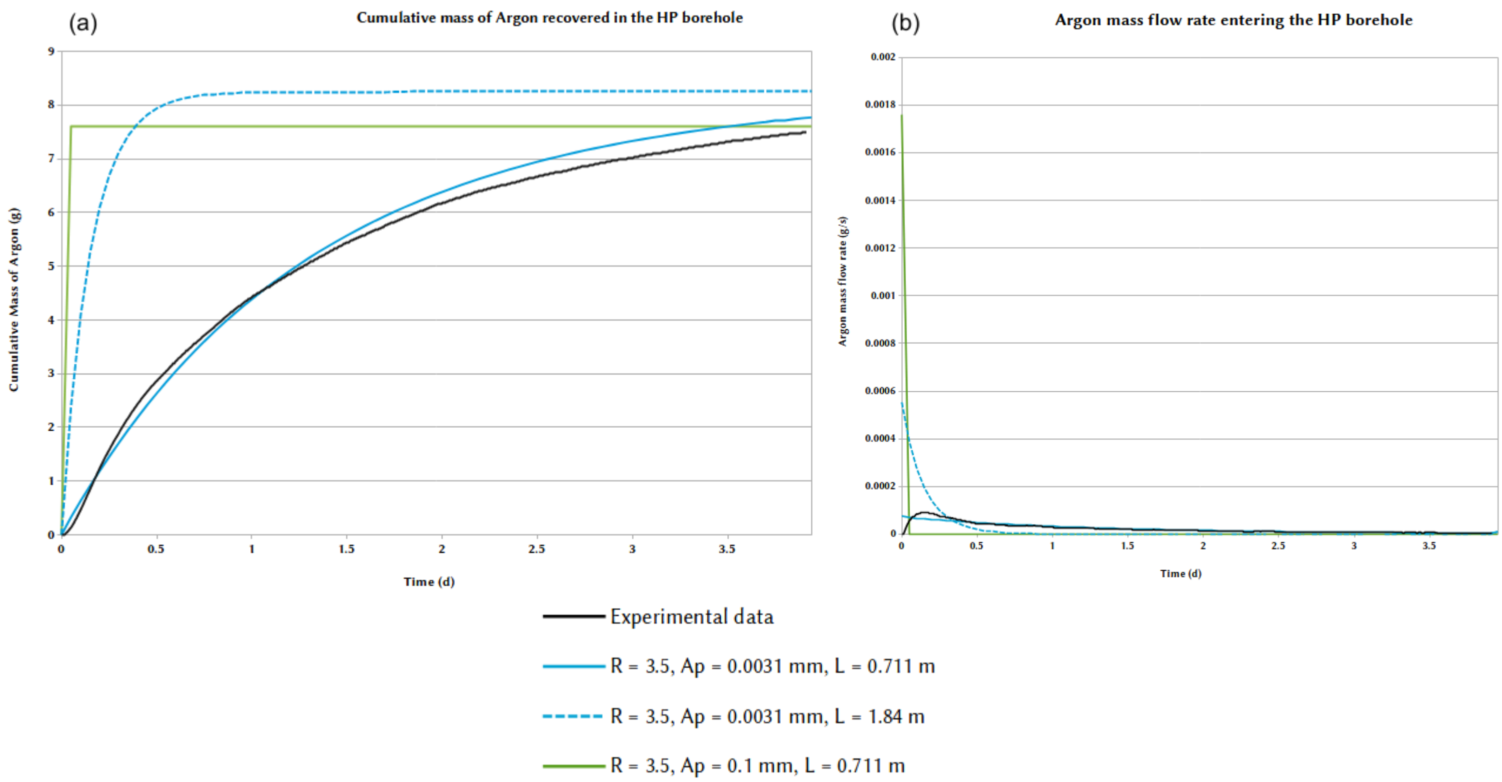

Figure 8. (a) Cumulative mass of argon gas entering the HP borehole over time, comparing experimental data (solid black line) with three model simulations (runs A, B and C) using R = 3.5 and varying length (L) and aperture (Ap). Run A (continuous blue line) yields approximately 7.77g of argon added to the HP borehole during the non-heated Step 1a, run B (dashed blue line) resulted in 8.24 g, and run C (continuous green line) in 7.61g. The mass of argon that entered the borehole during the three runs is higher than the experimental cumulative mass of argon. (b) Argon mass flow rate, in g/s, for the runs A, B and C. A zoomed-in figure of the simulation's start (0 to 0.5 days) is shown in the Appendix as Figure A14.

5.3. Modelling Step 1b: Thermomechanical permeability model

Step 1b turns the heater on and activates the permeability-aperture coupling. The same parameter combinations are evaluated: runs A, B and C. The description of each run's parameter set can be found in section 5.2.2. A methodological limitation applies to all three runs: in the physical experiment, the D borehole was repressurized to 20.8 psi approximately 25 minutes before the heater was switched on. Hence, a brief period of unheated gas breakthrough preceded the onset of heating. In the model, repressurization and heater activation occur simultaneously at t = 0, so it does not capture the short pre-heating decay. The practical consequence is minor; 25 minutes corresponds to approximately 0.017 days, and the calibrated fracture transmissivity produces only a small pressure drop over that interval; but it introduces a systematic offset in the early-time pressure record relative to the experimental data.

5.3.1. Full heating and cooling cycle using the best fit calibrated parameters

Due to high computational costs, only the best-fit parameter set (run A) is compared across the entire Step 1b time window. Figure 9 shows the D borehole pressure and temperature modelled over the full heating period and later second argon breakthrough window for run A (continuous black line; calibrated best fit), alongside the experimental pressure record. At t = 0, the D borehole is initialized at 244.74 kPa absolute (20.8 psi, gauge), and temperature throughout the domain is 301.15 K. As the heater power increases, the salt surrounding the HP borehole expands thermally. The hydraulic consequence is immediately visible: rather than decaying as in Step 1a, the D borehole pressure rises during the heating period, increasing from approximately 248 kPa at heating onset to a plateau of approximately 255 - 256 kPa by around day 30, and remaining elevated through to heater shutoff at day 56.

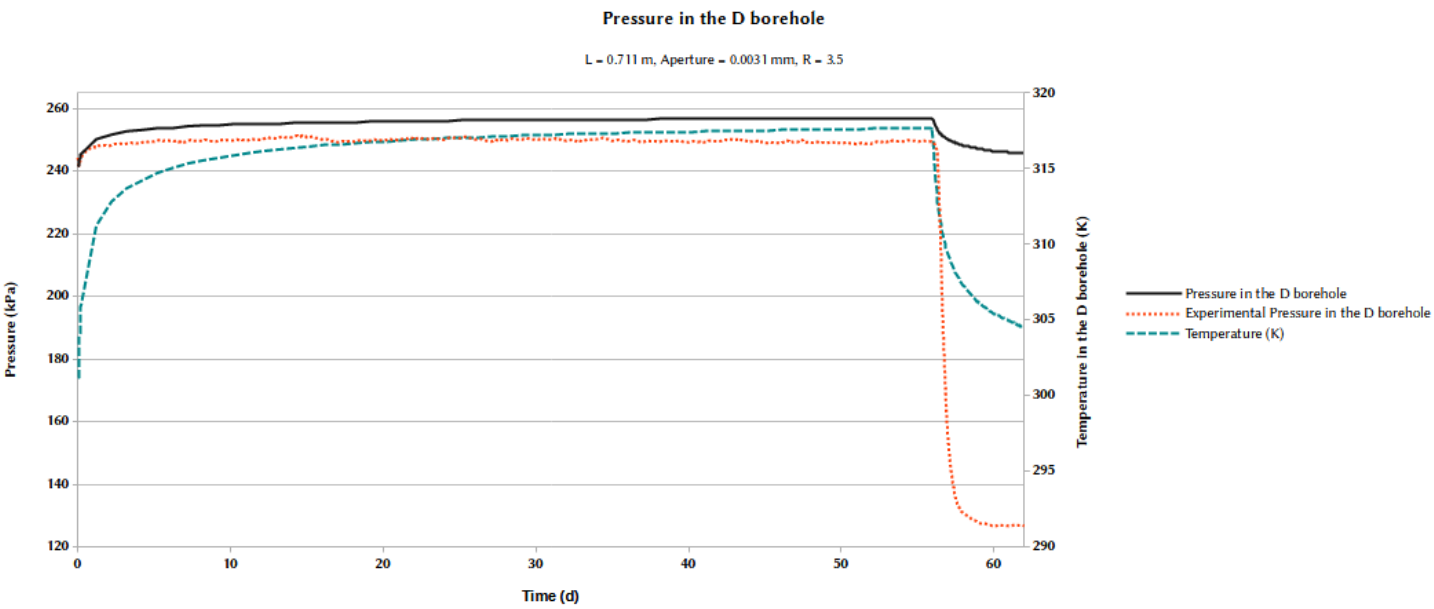

Figure 9. D borehole pressure and temperature (dashed blue line) over the full Step 1b simulation window for run A (continuous black line; calibrated parameter set: L = 0.711 m, Ap = 0.0031 mm, R = 3.5), compared against the experimental pressure record. The modelled pressure plateaus during

heating but, unlike the experimental data (dotted orange line), fails to reproduce the large post-heating pressure release upon heater switch-off at day 56 (see discussion in Section 6.1.2).

Once heating stops at day 56, modelled temperature begins to decrease; mechanical stress at the fracture relaxes, and the D borehole pressure drops from approximately 255 kPa to around 245 kPa over the following days. This diverges from the experimental results, where the pressure in the D borehole drops from approximately 250 kPa to approximately 128 kPa; a release of about 122 kPa (Appendix, Fig. A10). This difference in the post-heating depressurization is discussed further in Section 6.1.2.

5.3.2. Capturing the heating onset

Figure 10 focuses on the first half-day of Step 1b, during which the experimental data show that argon flow at HP ceases within approximately 70 minutes of heating onset. All three runs (A, B, and C) start at 241.29 kPa (20.3 psi gauge), and the divergence in their pressure decreases reflects differences in their fracture parameters.

Run A (continuous blue line) maintains a pressure that rises slightly from 241 kPa to approximately 247 kPa over the modelled 0.5 days, closely following the experimental pressure trend. Indeed, run A reproduces the experimental observations: the cessation of gas flow from D and an increase in pressure.

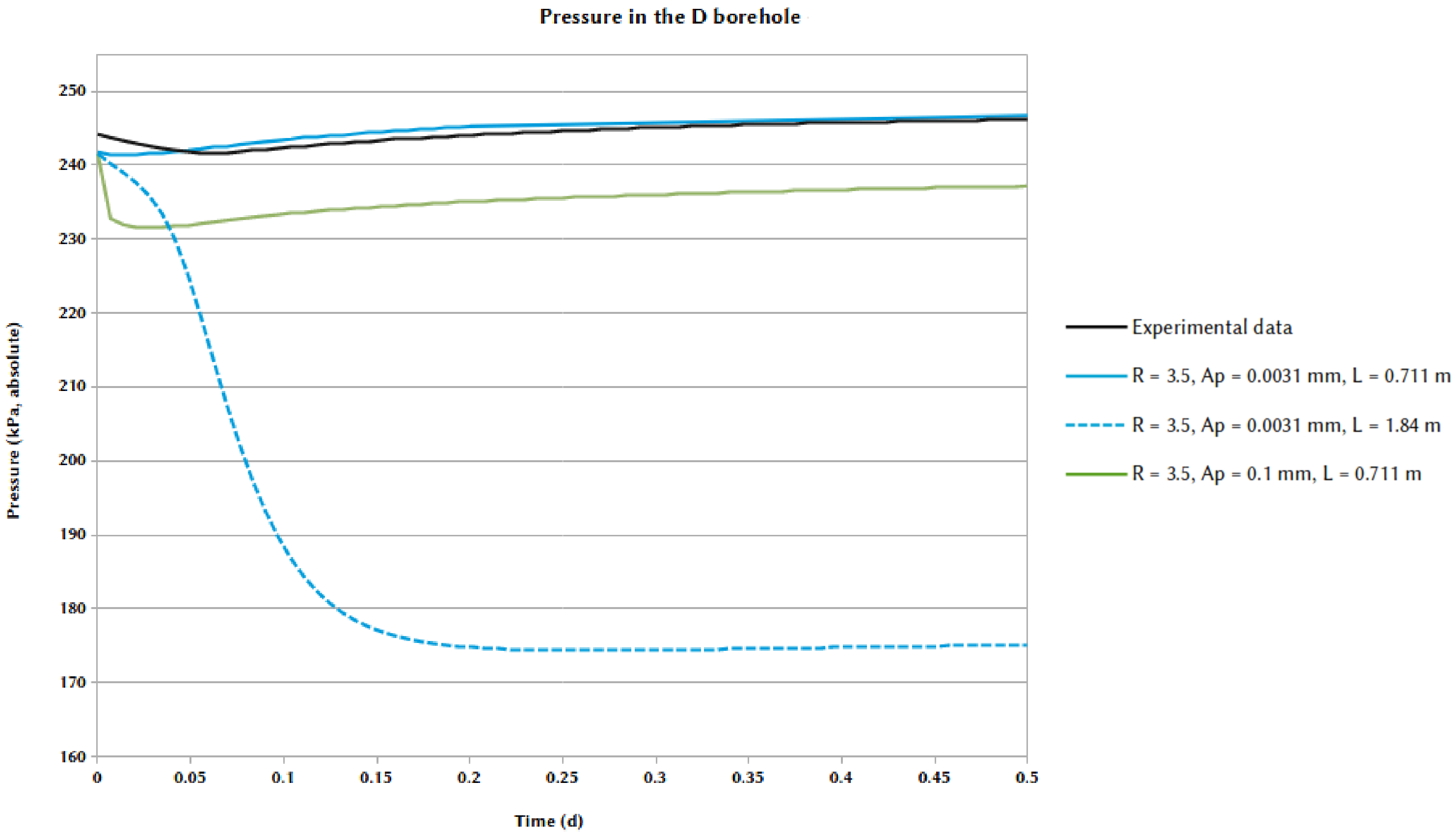

Figure 10. D borehole pressure (absolute) during the first 0.5 days of heating (Step 1b) for run A (continuous blue line; R = 3.5, Ap= 0.0031 mm, L = 0.711 m), run B (dashed blue line; same R and aperture, L = 1.84 m), and run C (continuous green line; same R and L = 0.711 m, Ap= 0.1 mm), compared against the experimental pressure record. Run A most closely reproduces the rapid pressure rise and argon flow cessation observed within ~0.05 days of heating onset, but all runs showcase an increase in pressure in the D borehole once argon flow was stopped.

Run B (dashed blue line) shows a similar behaviour; however, the initial pressure decay is larger than run A. It drops to approximately 175 kPa, and starts slightly increasing after. The longer fracture length results in more gas escape before aperture closure.

Finally, run C (continuous green line) represents an intermediate between the two other runs. The initial aperture is almost two orders of magnitude larger than run A, giving a permeability k_0 roughly four orders of magnitude higher. Although thermal closure does reduce the aperture, the cubic-law permeability remains orders of magnitude above the threshold needed to allow gas migration. As a result, D borehole pressure decays from 241 kPa to approximately 238 kPa over the first 0.5 days.

6. Discussion

6.1. Task 1a: Hydraulic modelling of tracer gas migration between boreholes

The pre-heating simulation (Step 1a) reproduces the overall behaviour of argon migration between the D and HP boreholes across all parameter sets. Still, the comparison with experimental data reveals discrepancies that highlight both model limitations and the physical complexity of the gas flow system between the two boreholes.

6.1.1. Modelling objectives 1 and 2: Pressure decay in the D borehole and mass of argon leaving the D borehole

The parameter sensitivity runs confirm that the pressure decay alone does not constrain the fracture geometry. As demonstrated by run A, a smaller and rougher fracture matches the pressure decay under ambient conditions (Step 1a). Additionally, varying fracture length in run B showed that a longer fracture increases overall transmissivity, causing the system to reach pressure equilibrium faster than in the experimental data. This mismatch in run B indicates that the fracture must be spatially constrained to avoid an overly rapid pressure decay in the D borehole. While different combinations of the roughness factor and aperture size that yield the same reference permeability (k_0) produce nearly identical pressure curves, mass-balance calculations provide an independent constraint (Appendix, Fig. A13).

Furthermore, lower fracture-plane roughness and longer fracture length will also allow faster equilibrium through increased transmissivity. The best-fit parameters result in an initial aperture's permeability of approximately $2.3 * 10^{-13} m^2$, which sits just above the range reported for heavily damaged salt (10^{-16} to $10^{-14} m^2$; Stormont et al., 1991; Lyu et al., 2022). This elevated value reflects what is being represented: not a distributed damage zone, but a well-connected fracture whose transmissivity is governed by aperture and roughness rather than by matrix microcracking.

The model calculates a maximum of approximately 8.2 g of argon leaving the D borehole across the modelled parameter sweep. This upper bound reflects how much gas the

D interval can store and the pressure difference driving flow. The experimental value of approximately 7.58 g removed from D by the end of Step 1a is consistent with this upper bound. Its closest match is the calibrated run A (~7.79 g), while R = 1 overshoots and R = 8 undershoots, providing the mass-balance corroboration for the pressure-based calibration choice.

Overall, modeling objectives 1 and 2 confirm that a single discrete fracture with a small aperture (in this study, Ap = 0.0031 mm) is sufficient to reproduce the observed pre-heating argon migration rates and mass transfer, demonstrating that even minimal hydraulic connectivity between boreholes - connectivity plausibly created by drilling-induced damage in a repository - is capable of supporting significant gas transport across short inter-borehole distances under ambient conditions alone.

6.1.2. Modelling objectives 3 and 4: Argon mass flow rate and cumulative argon mass entering the HP borehole

The modelled argon mass flow rates decay too quickly following the initial peak, indicating that the modelled fracture equilibrates fast once the pressure gradient decreases. However, the magnitude of this initial peak varies with geometry. Run C (larger initial aperture) produced an initial mass flow rate peak orders of magnitude higher than the experimental breakthrough trend. This demonstrates that increasing the initial aperture to recreate the full gas breakthrough profile creates an unrealistically conductive initial pathway. Instead, the tightly constrained initial peak in run A indicates that the physical pathway must be initially restricted.

Because fracture transmissivity scales with the square of the aperture, this relationship is the primary amplification mechanism driving the rapid, complete shutoff of the gas pathway within the observed 70-minute window. Additionally, the persistent underestimation of the decay tail across all runs compared to the experimental trend suggests that while a single tight fracture (run A) captures the initial bottleneck, a single fracture underestimates the effective contact area along the HP wall, which is consistent with a distributed EDZ microfracture network (Borns & Stormont, 1988; Kuhlman et al., 2024b). Additionally, the cumulative mass results introduce uncertainty in run C, which shows a 0.83 g mass-balance violation. This indicates that the pressure-based integration method for HP cumulative mass overestimates cumulative HP mass for the large-aperture scenario. Unlike runs A and B, run

C's larger aperture (Ap = $1 * 10^{-4} m$) creates a larger storage volume within the fracture itself, sustaining a larger pressure gradient and increasing compressive gas redistribution (Tounsi et al., 2023a). In the model, cumulative mass is derived from the HP pressure rise using the ideal gas law, $m = PVM/(RT)$, integrated over the borehole volume. The HP borehole was assigned an effective porosity of 0.7 to account for the volume of the heater, packer, and instrumentation; this porosity scales the gas-accessible volume. Because the calculated mass scales with the borehole volume, any overestimation of the effective void volume leads to an overestimation of the cumulative mass. The experimental mass, instead, is measured directly from argon concentration in the sampled HP gas stream, avoiding this volumetric uncertainty. The mass balance violation in run C therefore highlights a limitation of the post-processing method: cumulative mass at HP cannot be reliably computed from pressure integration alone when fracture storage is significant; the mass balance method (D mass loss - fracture storage) could be used instead (COMSOL Inc., 2023).

6.2. Physical interpretation of the shut-off mechanism

6.2.1. Closure mechanism and the pressure response

Heating rapidly closes the fracture in the model, as represented by the increasing D borehole pressure rather than the expected decay. As the salt around the HP borehole heats, it expands while confined by the surrounding rock, pushing inward on every free boundary within it, thereby narrowing the fracture (Section 4.2.3.2) and slightly reducing the borehole itself. Since the confined gas obeys the ideal gas law, both borehole volume reduction and gas heating increase pressure (Fig. 9; McTigue, 1986; McTigue & Nowak, 1987); both are also expected in the BATS-2g experiment itself. Furthermore, fracture closure reduces hydraulic conductance according to the cubic law (Witherspoon et al., 1980). Therefore, a greater fraction of the gas being compressed and heated is retained at the D borehole rather than migrating toward the HP borehole, accelerating the observed pressure rise.

Thermal closure is spatially heterogeneous (Appendix, Fig. A8). Normal compressive stress and inward displacement are the greatest at the fracture intersection closest to the heater, where temperatures are highest. This leads to the earliest reduction in aperture. Both temperature and compressive stress decrease toward the D borehole, delaying fracture closure and preserving a larger aperture.

Finally, in this model, thermal strain is the main driver of closure. With inelastic strain terms set to zero and no poroelastic coupling, the stress in the bulk salt follows the classical thermoelastic relation for a confined elastic solid (Boley & Weiner, 1960). Coupled THM modelling of heated salt boreholes confirms that thermal stresses peak near the heat source and follow the evolving temperature field (Tounsi et al., 2023a; Appendix, Fig. A8), and even moderate thermal strain at the HP end is sufficient to produce the near-complete permeability decrease the model reproduces.

6.2.2. The excavation damaged zone (EDZ)

Drilling perturbs the local stress field and produces an Excavation Damaged Zone (EDZ) in salt, where the otherwise near-impermeable matrix is pervaded by microfractures with elevated porosity and permeability extending several borehole radii from the wall (Tsang et al., 1991; Stormont et al., 1991; Kuhlman, 2024). The D-HP connection was therefore likely never a single clean fracture, but a network of interconnected microfractures whose collective response to heating and cooling would not follow the same simple, single-valued aperture-cubed response as an idealized plane. During heating, the model reproduces experimental D borehole pressure well (Section 5.3), suggesting the calibrated single fracture serves, in that scenario, as an acceptable proxy for the EDZ's network closure behaviour.

This model diverges from the experiment after heating stops. During cooling, modelled D borehole pressure decreases only slightly (approximately 255 to 245 kPa) - whereas the experimental pressure experiences an approximate 125 kPa decrease over the same period (Appendix, Fig. A12). Elastic reopening of a single fracture cannot account for such a drop. Instead, cooling generates tensile stresses that reopen and extend microfractures within the EDZ (Tounsi et al., 2023a; Watson et al., 2025), increasing the combined hydraulic conductance of multiple flow paths. This process is amplified by dilatancy, which is not represented in this model. Dilatancy-induced microcracking can increase permeability by more than an order of magnitude near borehole walls (Tounsi et al., 2023a; Lyu et al., 2022), which helps explain the rapid pressure decline observed experimentally (Fig. 9; Appendix, Fig. A12).

This interpretation is supported by historical field and laboratory evidence. Large-scale tests at the Avery Island domal salt mine showed that fractured salt permeability decreases under heating as thermal expansion tightens intercrystalline porosity and closes micro- and macro-fractures in the disturbed zone (Blankenship et al., 1983), then increases by four to five orders of magnitude during the cooling phase (from $2.0 * 10^{-21} m^2$ to $1.2 * 10^{-16} m^2$), mirroring the post-heating pressure release observed in BATS (Kuhlman et al., 2017). Additional laboratory experiments on Asse rock salt at Delft University of Technology recorded a large decrease in P-wave velocity during cooling (Roest, 1984), indicating fracture development and larger mechanical damage during cooling than heating. Direct in situ confirmation also comes from acoustic emission (AE) monitoring in the BATS experiment. The first breakthrough of post-heating flow coincided with a spike in AE activity, and event rates during cooling were higher than those recorded during the heating phase (Kuhlman et al., 2024). Together, these observations indicate that the hydraulic response during cooling is governed by the evolution of a distributed fracture network rather than by the reversible elastic closure of a single plane.

6.3. Impacts of the model simplifications and recommendations for future work

The coupled model as presented relies on several simplifying assumptions whose effects on the results should be acknowledged.

6.3.1. Linear elasticity and the absence of viscoplastic creep

By largely focusing on the early, rapid phase (0.05 days) of the argon shutoff, the model relies entirely on instantaneous elastic deformation. This successfully captures the initial thermal shock because macro-scale viscoplastic strain in rock salt typically requires days to weeks to accumulate under repository stresses and temperatures (Krieg et al., 1984; Plúa et al., 2024).

However, neglecting inelastic deformation prevents the model from reproducing the progressive fracture sealing observed at longer timescales. In reality, viscoplastic creep continues to reduce fracture aperture after the initial thermoelastic response, maintaining a low permeability (Tounsi et al., 2023). Integrating a time-dependent constitutive law - such as a Norton-Bailey or Munson-Dawson creep - into the solid mechanics module would help improve this model, allowing the latter to capture the transition from a short-term thermoelastic closure to a long-term viscoplastic sealing (COMSOL Inc., 2023). Because creep alone cannot reproduce fracture reopening during cooling, it should be coupled with a dilatancy criterion that accounts for microcrack development once the stress state crosses the dilatancy boundary (Tounsi et al., 2023), as discussed in section 6.3.4.

6.3.2. Absence of poroelastic coupling and fracture surface idealization

The model does not include poroelastic effective stress coupling, so fracture closure is driven only by thermal expansion and unaffected by internal gas pressure. As a result, the spring constant must be calibrated to match the timing of the observed shutoff, rather than to reflect a physically resisted closure process; this simulation requires a high thermal driving force to achieve the observed shutoff and forces reliance on a global roughness factor R (Section 4.2.3.3). Previous studies show that incorporating Biot poroelastic coupling produces more realistic mechanical parameters and better reproduces both the heating and cooling responses in heated salt boreholes (Tounsi et al., 2023a; Watson et al., 2025). Therefore, implementing COMSOL's poromechanics coupling would allow gas pressure to resist the fracture's closure and reduce dependence on parameters in need of calibration.

Additionally, such use of a constant roughness factor neglects the actual geometry of the fracture surfaces. Gas migration through the EDZ concentrates along a tortuous network of channels rather than between two smooth parallel faces. As opposing faces approach contact under thermal expansion, non-uniform surface geometry leads to a more nonlinear collapse of hydraulic conductance than the cubic law predicts (Witherspoon et al., 1980; Yasuhara et al., 2004). Incorporating variable roughness, contact mechanics along the fracture length, and an evolving EDZ permeability field would further reduce dependence on a single global calibration parameter.

6.3.3. Impacts of the salt matrix impermeability

Assigning a zero permeability to the surrounding salt matrix confines all gas flow to the fracture, preventing lateral pressure dissipation into the EDZ. In reality, limited gas migration through the damaged zone would moderate pressure build-up during heating (Stormont et al., 1991; Lyu et al., 2022). This simplification likely contributes to the model's overestimation of the heating-phase pressure rise (Fig. 9); assigning a dynamic permeability to the EDZ would help fix that overestimation. A related limitation is the absence of brine vapour pressure: salt contains small amounts of mobile brine that migrate toward a heat source and partially vaporise near the 140°C experimental setpoint, adding a pressure contribution the model does not reproduce (Cline & Anthony, 1971; McTigue & Nowak, 1987), and which would further amplify the experimental pressure rise beyond what the two thermoelastic mechanisms alone predict.

6.3.4. Dilatancy omission and its consequences for post-heating pressure decay

The model omits dilatancy: the volumetric expansion and micro-cracking of rock salt under deviatoric stress. As discussed in Section 6.2.2, near the borehole walls the stress state can cross the salt dilatancy boundary, opening micro-pathways that compete with compressive thermal closure during heating and drive rapid network reopening during cooling. Because this mechanism is identified as the primary physical explanation for the post-heating pressure collapse, its absence from the model is the single most consequential limitation for reproducing the cooling-phase behaviour. Therefore, introducing a viscoplastic constitutive model capable of tracking dilatancy boundaries; building on the creep law recommended in Section 6.3.1; would address both the sustained sealing behaviour during heating and tensile microcrack extension during cooling within a unified rheological formulation (Lyu et al., 2022).

7. Conclusions

A fully coupled three-dimensional thermal-hydrological-mechanical (THM) model successfully reproduces the argon flow breakthrough and cessation observed during the WIPP BATS-2g experiment. Implementing a 3D geometry aligned the thermal component with reference benchmarks and allowed for the model results to match the four-day ambient pressure decay more accurately than a 2D model would.

The heated simulations demonstrate that localized thermoelastic expansion under rock confinement generates intense compressive normal stresses that can drive rapid and non-uniform fracture closure. Mechanical displacement and compressive stress peak at the borehole-fracture intersection closest to the heater array, which creates a near-zero-transmissivity bottleneck that severs the inter-borehole hydraulic connection even while sections of the fracture further from the heat source retain a residual aperture. The resulting aperture reduction decreases fracture transmissivity, forcing a pressure rise at the D borehole that mirrors the experimental data.

The parametric comparison across the three simulation runs confirms that the timing and completeness of shut-off are governed both by fracture length and initial aperture. An extended fracture geometry or a larger initial aperture cannot reproduce the observed timing of cessation. While an extended fracture geometry delays the decrease in flow rate, a larger aperture maintains transmissivity under thermal compression. Only the short, tight fracture configuration captures the precise shut-off timing and the sustained heating-phase pressure plateau; however, even this configuration fails to reproduce the subsequent post-heating pressure reversal. This has a direct implication for the safety case: thermoelastic closure alone is insufficient to guarantee hydraulic isolation. The same thermal perturbation that seals the pathway during heating can, upon cooling, generate tensile stresses that reopen a distributed fracture network with greater conductance than a single elastic plane can recover. This asymmetry means that the long-term integrity of a salt repository cannot be assumed from the heating-phase behaviour alone; it must be evaluated over the full thermal cycle, including the potentially more damaging cooling phase.

Future work within COPERA and DECOVALEX must therefore move beyond elastic models toward a coupled poro-visco-plastic formulation that captures dilatancy, creep, and EDZ evolution - because hydraulic isolation, and with it the long-term safety of a salt-hosted repository, relies on whether the salt's thermal response is a permanent seal or a temporary one.

References

Anthony, T. R., & Cline, H. E. (1971). Thermal migration of liquid droplets through solids. *Journal of Applied Physics*, *42*(9), 3380–3387. https://doi.org/10.1063/1.1660741

Bartol, J., & Vuorio, M. (2025). Safety assessment for a geological disposal facility in domal salt: The Dutch case. *Geomechanics for Energy and the Environment*, *41*, 100645. https://doi.org/10.1016/j.gete.2025.100645

Birkholzer, J.T., Bond, A.E. & Tsang, C. (2024). The DECOVALEX international collaboration on modelling of coupled subsurface processes and its contribution to confidence building in radioactive waste disposal. Hydrogeol J 32, 1295ß1305. https://doi.org/10.1007/s10040-024-02799-7

Blankenship, D. A. (1983). *Nitrogen Gas Permeability Tests At Avery Island: Technical Report*. Columbus, OH: The Office.

Boley, B. A., & Weiner, J. H. (1960). *Theory of thermal stresses*. John Wiley & Sons.

Borns, D. J., & Stormont, J. C. (1988). An interim characterization of the excavation effect zone at the Waste Isolation Pilot Plant: The evolution of understanding. *Rock Mechanics and Rock Engineering*, *22*(4), 327-345.

Bruno, M. S. (2002). Geomechanical and decision analyses for mitigating compaction-related casing damage. *SPE Drilling & Completion*, *17*(3), 179-188. https://doi.org/10.2118/79519-PA

Chase, M. W. (1998). *NIST-JANAF Thermochemical Tables, Fourth Edition*. 1-1951.

Commissie Opberging Radioactief Afval. (2001). *Berging van radioactief afval: Advies van de Commissie Opsberging Radioactief Afval*. Ministry of Housing, Spatial Planning and the Environment.

COMSOL Inc. (2023). *COMSOL Multiphysics reference manual, version 6.2*. COMSOL AB.

COVRA. (2025). *Jaarrapport 2024*. Centrale Organisatie Voor Radioactief Afval N.V.

Ministry of Climate and Green Growth. (2024). *Letter from the Minister of Climate and Green Growth* (No. 132, 32,645 Nuclear energy) (Letter to the Speaker of the House of Representatives of the States General). Parliamentary Documents.

Lauwerier (2022). Evolution of Zechstein salt diapirs in the North-Eastern Netherlands (Internship report), Utrecht University.

IAEA. (2011). Disposal of radioactive waste: Specific safety requirements (IAEA Safety Standards Series No. SSR-5). *International Atomic Energy Agency*.

Krieg, R., Stephenson, D. J., Branstetter, L. J., Stone, M., Wawersik, W., & Moore, N. Y. (1984). Reference stratigraphy and rock properties for the Waste Isolation Pilot Plant (WIPP) project. Sandia National Laboratories.

Kuhlman, K. L., Mills, M. M., & Matteo, E. N. (2017). Consensus on intermediate scale salt field test design (SAND2017-3179R; SFWD-SFWST-2017-000099). Sandia National Laboratories, US Department of Energy Spent Fuel and Waste Science and Technology.

Kuhlman, K. L., Mills, M. Marie, Jayne, Richard Scott, Matteo, Edward N., Herrick, Courtney G., Choens, Robert Charles, Paul, Matthew J., Stauffer, Phiip H., Guiltinan, Eric, Rahn, Thom, Otto, Shawn, Davis, Jon, Eldridge, Daniel L., Rutqvist, Jonny, Wu, Yuxin, Hu, Mengsu, Chen, Hang, & Wang, Jiannan (2024). Brine Availability Test in Salt (BATS) FY24 Update. https://doi.org/10.2172/2462942

Kuhlman, K. L., Bartol, J., Benbow, S. J., Bourret, M., Czaikowski, O., Guiltinan, E., Jantschik, K., Jayne, R., Norris, S., Rutqvist, J., Shao, H., Stauffer, P. H., Tounsi, H., & Watson, C. (2024b). Synthesis of results for Brine Availability Test in Salt (BATS) DECOVALEX-2023 Task E. *Geomechanics for Energy and the Environment*, *39*, 100581. https://doi.org/10.1016/j.gete.2024.100581

LaForce, T., Bartol, J., Becker, D.-A., Benbow, S., Bond, A., Dietl, C. R., Frank, T., Kock, I., Magri, F., Nicholas, J., Jayne, R., Pekala, M., Stauffer, P. H., Stein, E., Stone, J., & Wolf, J. (2024). Comparing modelling approaches for a generic nuclear waste repository in salt. *Geomechanics for Energy and the Environment*, *40*, 100621. https://doi.org/10.1016/j.gete.2024.100621

Lauwerier, W. (2022). Evolution of the Zechstein salt diapirs in the north-eastern Netherlands (Internship Report). Utrecht University & COVRA N.V.

Li, M., Collard, N., Schueller, S., Matenco, L., Nader, F. H., Beekman, F., Cacas, M.-C., & Bartol, J. (2024). Quantitative modelling of diapirism and geochemical evolution of the subrosion process of salt domes in the northeast Netherlands for radioactive waste disposal (Project Report). Utrecht University & IFP Energies Nouvelles.

Little, W. J. (1964). Tables of thermodynamic properties of argon from 100 to 3000°K (Technical Documentary Report No. AEDC-TDR-64-68). Arnold Engineering Development Center, Air Force Systems Command, United States Air Force.

Lyu, C., Liu, J., Ren, Y., Liang, C., & Zeng, Y. (2022). Mechanical characteristics and permeability evolution of salt rock under thermal-hydro-mechanical (THM) coupling condition. *Engineering Geology*, *302*, 106633. https://doi.org/10.1016/j.enggeo.2022.106633

McTigue, D. F. (1986). Thermoelastic response of fluid-saturated porous rock. *Journal of Geophysical Research: Solid Earth*, *91*(B9), 9533–9542. https://doi.org/10.1029/JB091iB09p09533

McTigue, D. F. (1990). Flow to a heated borehole in porous, thermoelastic rock: Analysis. *Water Resources Research*, *26*(8), 1763–1774. https://doi.org/10.1029/WR026i008p01763

McTigue, D. F., & Nowak, E. J. (1987). Brine and gas transport processes in rock salt: A coupled analysis (SAND87-1990). Sandia National Laboratories.

Mills, M. M. (2016). Characterization of consolidated granular salt (Master's thesis). University of New Mexico. *UNM Digital Repository*. http://hdl.handle.net/1928/32967

National Research Council. (1996). The Waste Isolation Pilot Plant: A potential solution for the disposal of transuranic waste. *The National Academies Press*. https://doi.org/10.17226/5269

NEA. (2020). Geological disposal of radioactive waste: National programmes and progress. *Nuclear Energy Agency*, OECD.

Office of Nuclear Waste Isolation. (1981). Physical properties of WIPP salt. *UNT Digital Library.* https://digital.library.unt.edu/ark:/67531/metadc1313308/

Office of Nuclear Waste Isolation. (1988). Brine inflow model for WIPP. IAEA. https://inis.iaea.org/search/

Ottenheim, S. (2025). Influence of Temperature-Dependent Specific Heat and Conductivity on Heat and Gas Migration in Rock Salt: A Computational Study within BATS II (MSc thesis). Utrecht University.

Plúa, C., De La Vaissière, R., Armand, G., Olivella, S., Rodríguez-Dono, A., Yu, Z., Shao, J., Radeisen, E., & Shao, H. (2025). Numerical investigation of the gas-induced fracturing behaviour of the Callovo-Oxfordian claystone. *Geomechanics for Energy and the Environment*, *42*, 100669. https://doi.org/10.1016/j.gete.2025.100669

Roest, J. Acoustic P-wave velocity measurements of cataclastic effects in rock salt (1984). EUR 10857 EN, *Nuclear Science and Technology Commission of the European Communities*, Brussels, Belgium.

Stormont, J. C., Howard, C. L., & Daemen, J. J. K. (1991). In situ measurements of rock salt permeability changes due to nearby excavations (SAND90-3134). Sandia National Laboratories. https://doi.org/10.2172/6244387

Tounsi, H., Rutqvist, J., Hu, M. et al. (2023). Long-term sinking of nuclear waste canisters in salt formations by low-stress creep at high temperature. *Acta Geotech.* **18**, 3469–3484. https://doi.org/10.1007/s11440-023-01900-w

Tounsi, H., Rutqvist, J., Hu, M., & Kuhlman, K. (2023a). Coupled THM modelling of a heated borehole in rock salt: Thermally driven stress, permeability evolution, and dilatancy boundary crossing. *International Journal of Rock Mechanics and Mining Sciences*, *168*, 105405.

Tsang, C.-F. (1991). Coupled hydromechanical-thermochemical processes in rock fractures. *Reviews of Geophysics*, *29*(4), 537–551. https://doi.org/10.1029/91RG01832

Van der Veen, G., Scholten, C., & Buitenhuis, A. (2018). Beknopte evaluatie van OPERA: Onderzoeksprogramma voor de Eindberging van Radioactief Afval. *Technopolis Group Amsterdam*.

Watson, C., Benbow, S., Bond, A., Norris, S., & Parsons, S. (2025). A simple model to represent damage and fracturing in rock salt caused by heating and subsequent cooling: Understanding brine inflow data from the Brine Availability Test in Salt (BATS). *Geomechanics for Energy and the Environment*, *41*, 100646. https://doi.org/10.1016/j.gete.2025.100646

Witherspoon, P. A., Wang, J. S. Y., Iwai, K., & Gale, J. E. (1980). Validity of Cubic Law for fluid flow in a deformable rock fracture. *Water Resources Research*, *16*(6), 1016–1024. https://doi.org/10.1029/WR016i006p01016

Yasuhara, H., Polak, A., Mitani, Y., Grader, A. S., Halleck, P. M., & Elsworth, D. (2006). Evolution of fracture permeability through fluid–rock reaction under hydrothermal conditions. *Earth and Planetary Science Letters*, *244*(1), 186–200. https://doi.org/10.1016/j.epsl.2006.01.046

Appendix

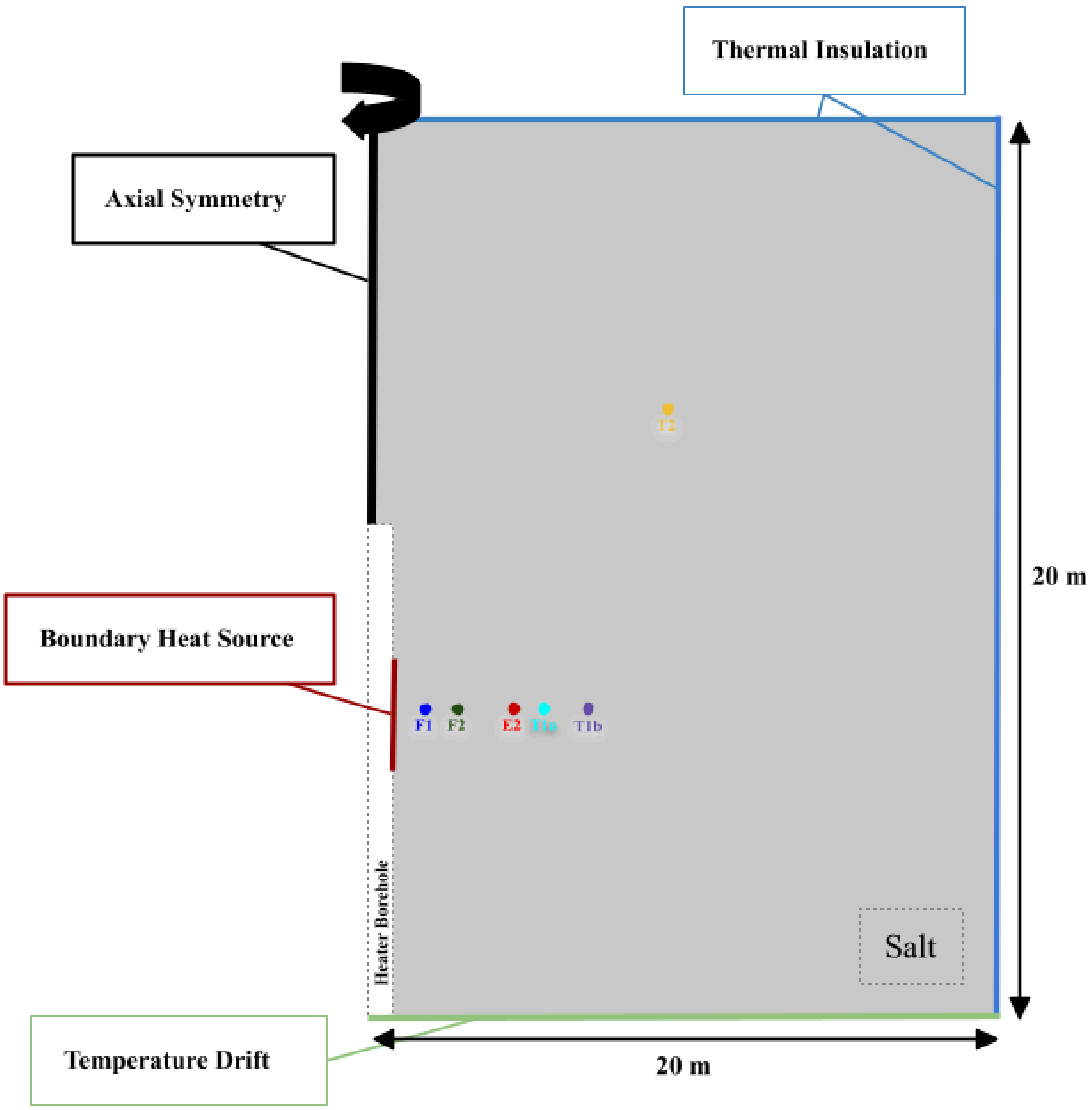

Figure A1. Geometry and boundary conditions of the 2D axisymmetric thermal benchmark model, reproduced from Ottenheim (2025). The domain measures 20 m × 20 m, with axial symmetry along the heater borehole centreline, thermal insulation on the outer boundaries, a temperature-drift condition at the drift-facing boundary, and a boundary heat source representing the HP heater. The sensors are modelled using their radial distance from the heater.

Table A1. Spatial coordinates of the six sensor positions used for the thermal benchmark (top), and the radius, height, and centreline coordinates of the HP borehole, heater, and D borehole as implemented in the 3D model geometry (bottom).

Sensor	X (m)	Y (m)	Z (m)
HE2RTD3	-0.548	2.972	0
HF1TC2	-0.193	2.972	0
HF2TC3	-0.289	2.972	0
T1TC10	-0.979	2.972	0
T1TC15	-1.875	4.572	0
T2TC10	-0.688	2.972	0

Element	Radius (m)	Height (m)	X-coordinate (m)	Y-coordinate (m)	Z-coordinate (m)
HP borehole	0.06095	1.84	0	1.98	0
Heater	0.06095	0.711	0	2.616	0
D borehole	0.02665	3.052	0	1.53	0

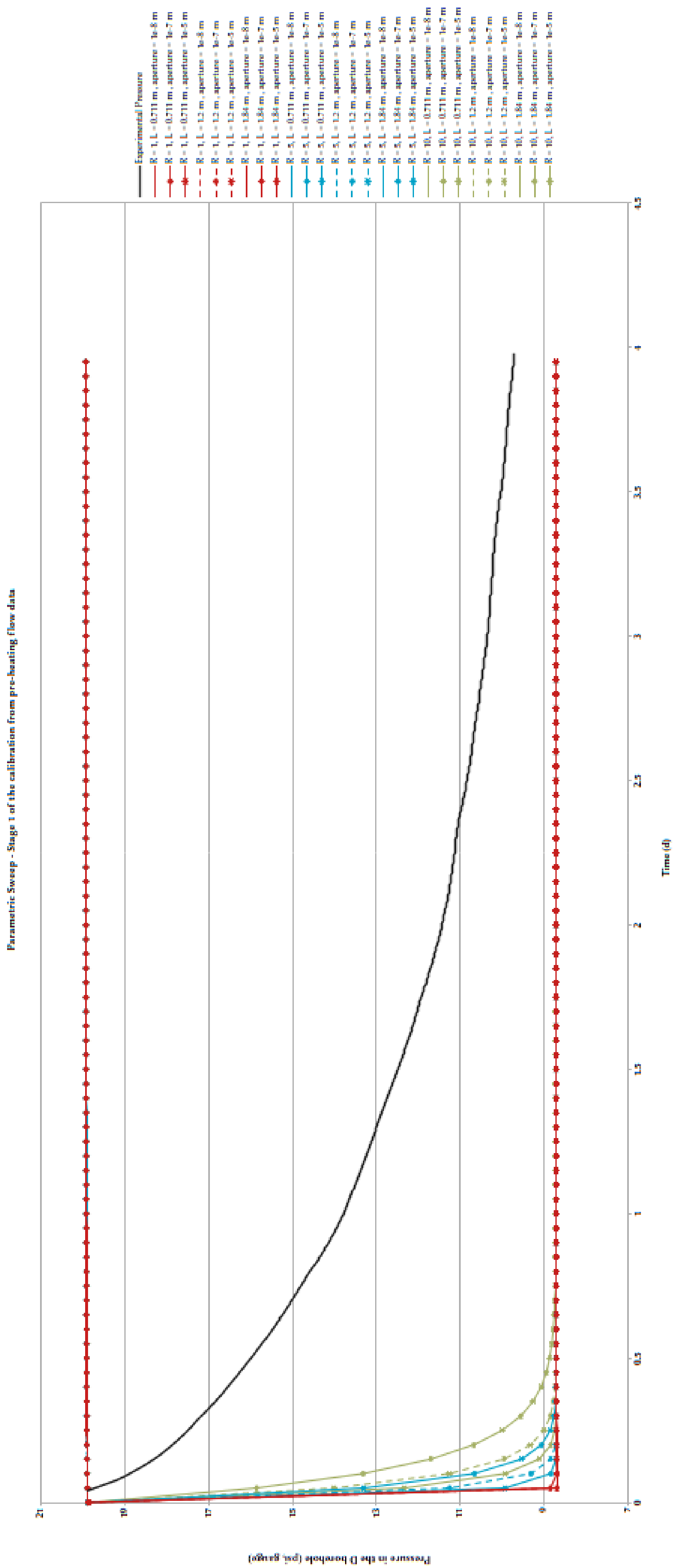

Figure A2. Parametric sweep: Stage 1. This sweep was performed to constrain the parameters R (1, 5 & 10), L (0.711, 1.2, and 1.84 m), and $Ap_0\,(1 * 10^{-8}, 1 * 10^{-7}, 1 * 10^{-5})$.

Figure A3. Parametric sweep: Stage 2. This sweep was performed to constrain the parameters R (1, 5, 8,10), L(0.711m) and

$Ap_0\ (1 * 10^{-5}, 5 * 10^{-6}, 1 * 10^{-6}, 5 * 10^{-7} m).$

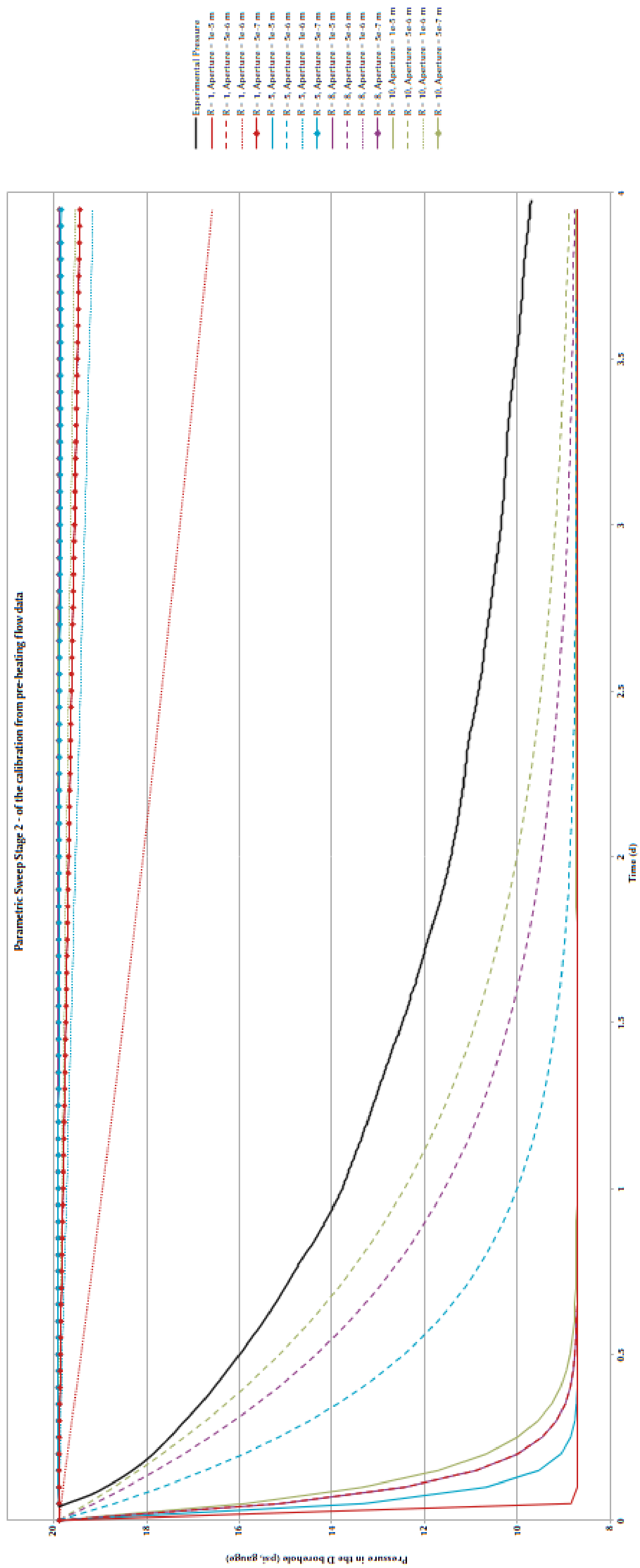

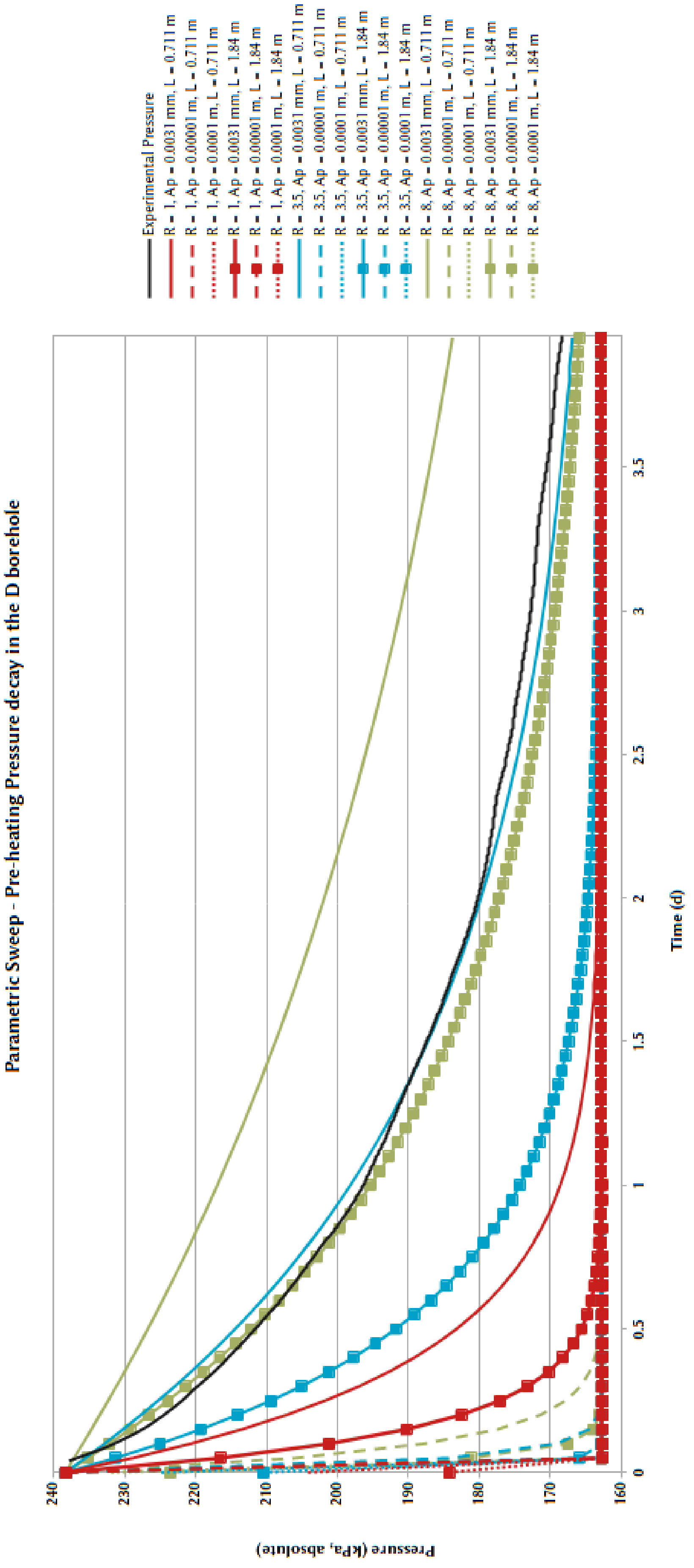

Figure A4. D borehole pressure decay during the pre-heating period (Step 1a) for the complete refined parameter sweep (Stage 2 of calibration; Section 5.1), spanning roughness factors R = 1, 3.5, and 8, apertures from $1 * 10^{-4}$ *to* $3.1 * 10^{-6}$*m, and fracture lengths L = 0.711 m and 1.84 m, compared against the experimental pressure record. The calibrated set (R = 3.5, aperture = 0.0031 mm, L = 0.711 m) most closely tracks the experimental curve across the full 4-day window.*

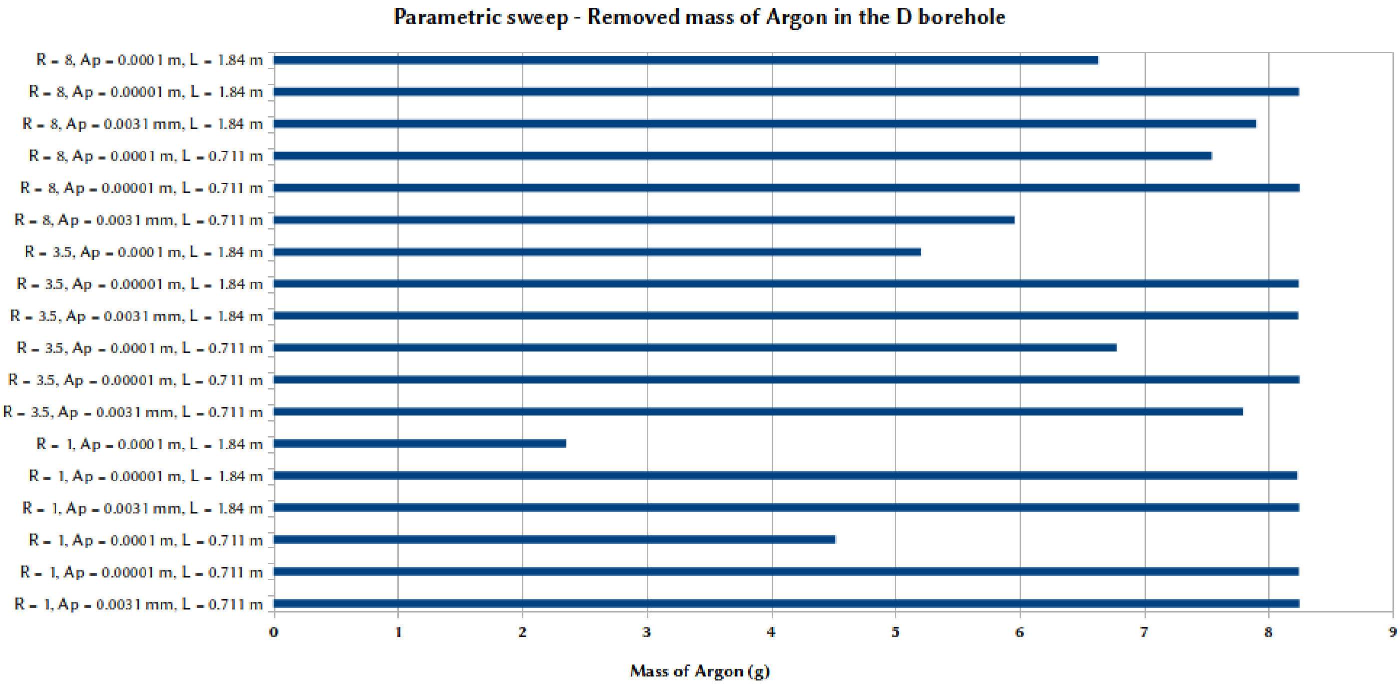

Figure A5. Cumulative mass of argon removed from the D borehole by the end of Step 1a for each combination in the refined parameter sweep (R = 1, 3.5, 8; aperture = $1 * 10^{-4}$ *to* $3.1 * 10^{-6}$ *m; L = 0.711 m and 1.84 m). Lower-roughness and longer-fracture combinations approach hydraulic equilibrium fastest, consistent with the pressure decay trends in Figure 5.*

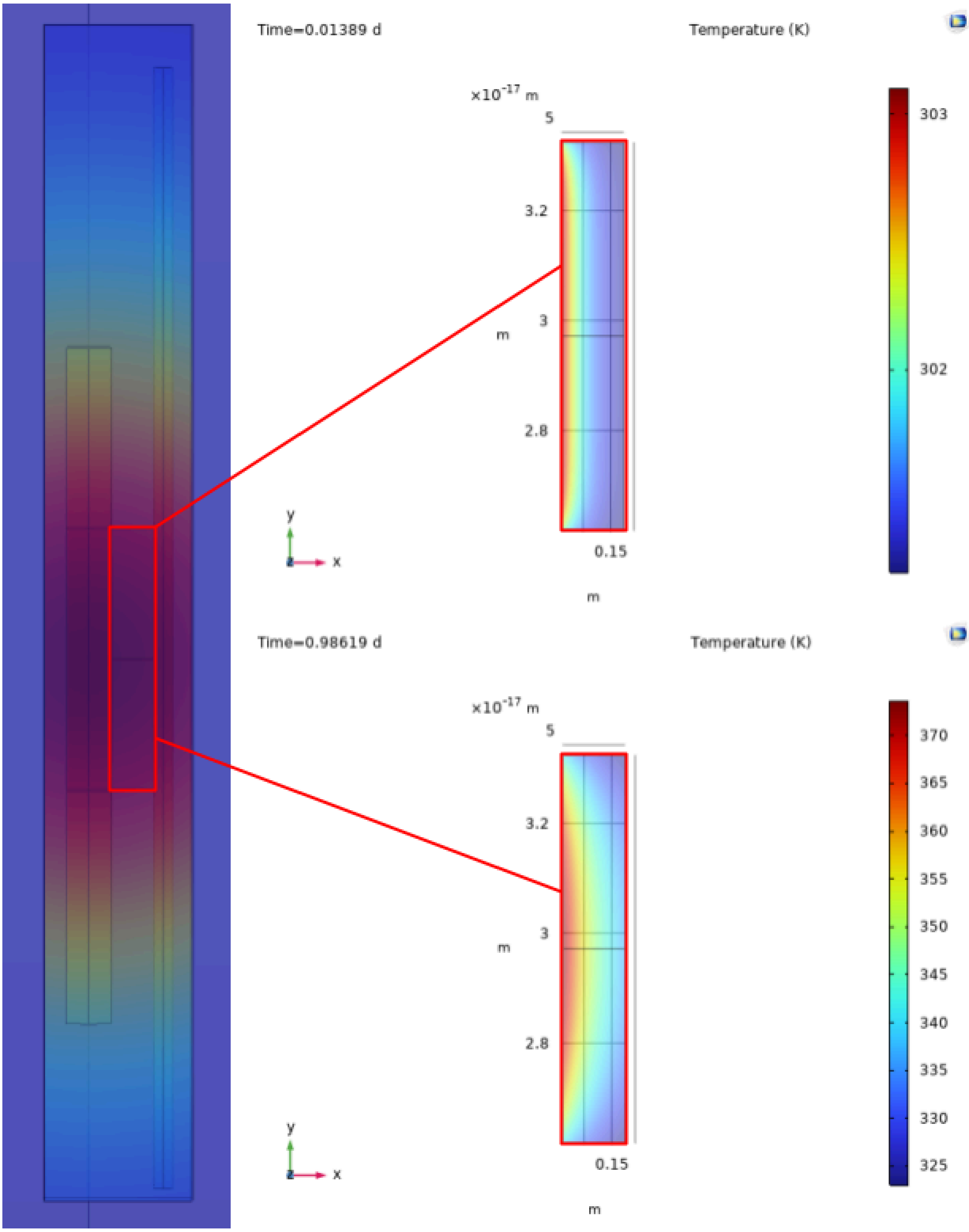

Figure A6. Evolution of the thermal field around the HP borehole following heater activation (Step 1b, t = 0.01 d) and after one day of heating (Step 1b, t = 0.99 d). Insets show a zoomed cross-section of the fracture region between the HP and D boreholes (fracture length L = 0.711 m), showcasing the rapid temperature rise concentrated near the heater.

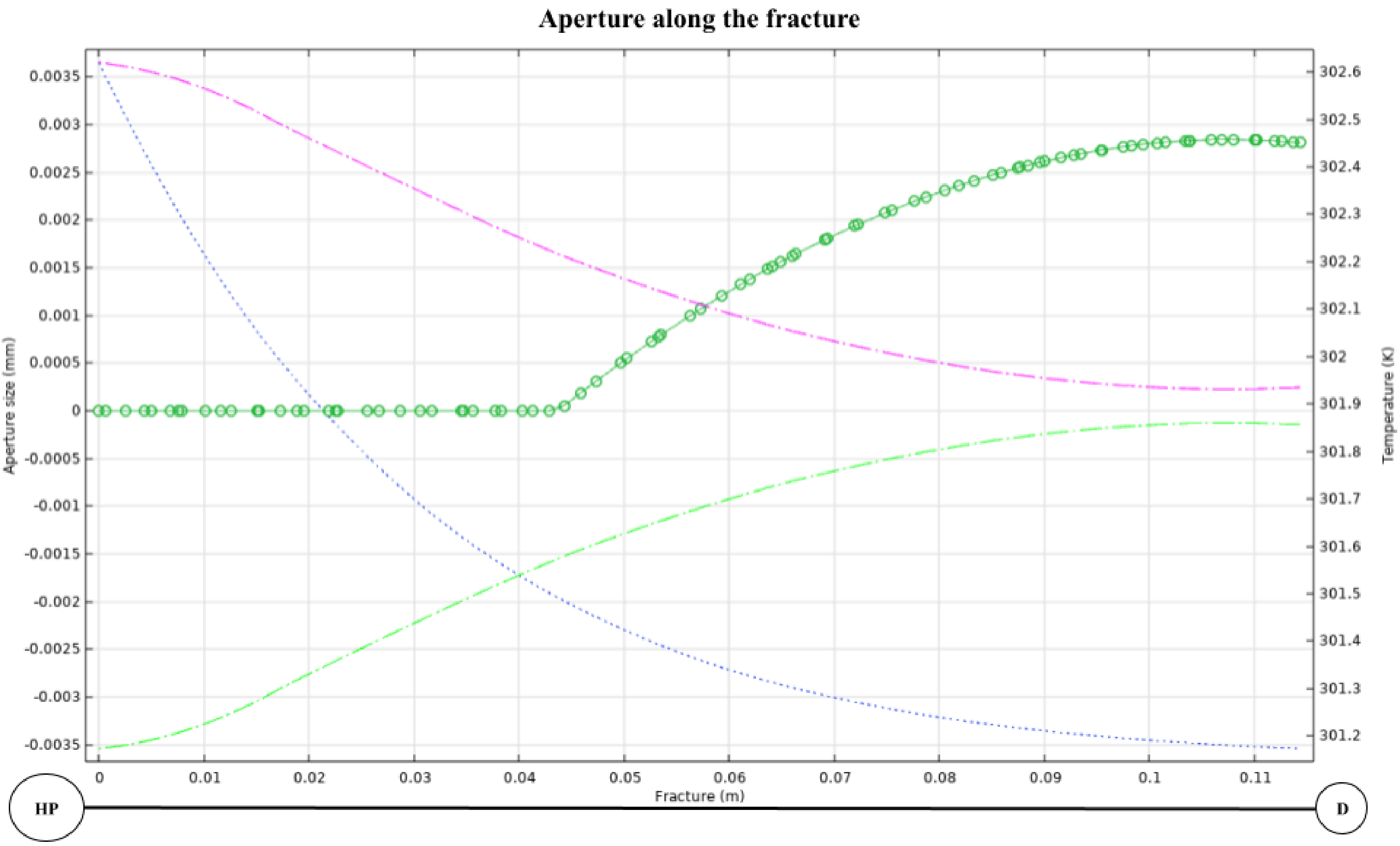

Figure A7. Modelled aperture and temperature profile along the fracture length at t = 0.5 days, from the HP borehole contact (0 m, left) to the D borehole contact (right). The magenta and green lines show, respectively, the normal displacement of the lower and upper fracture faces, while the blue dotted line represents the temperature profile; aperture closure is most pronounced near the HP end, consistent with the localized thermal loading described in Section 6.1.1.

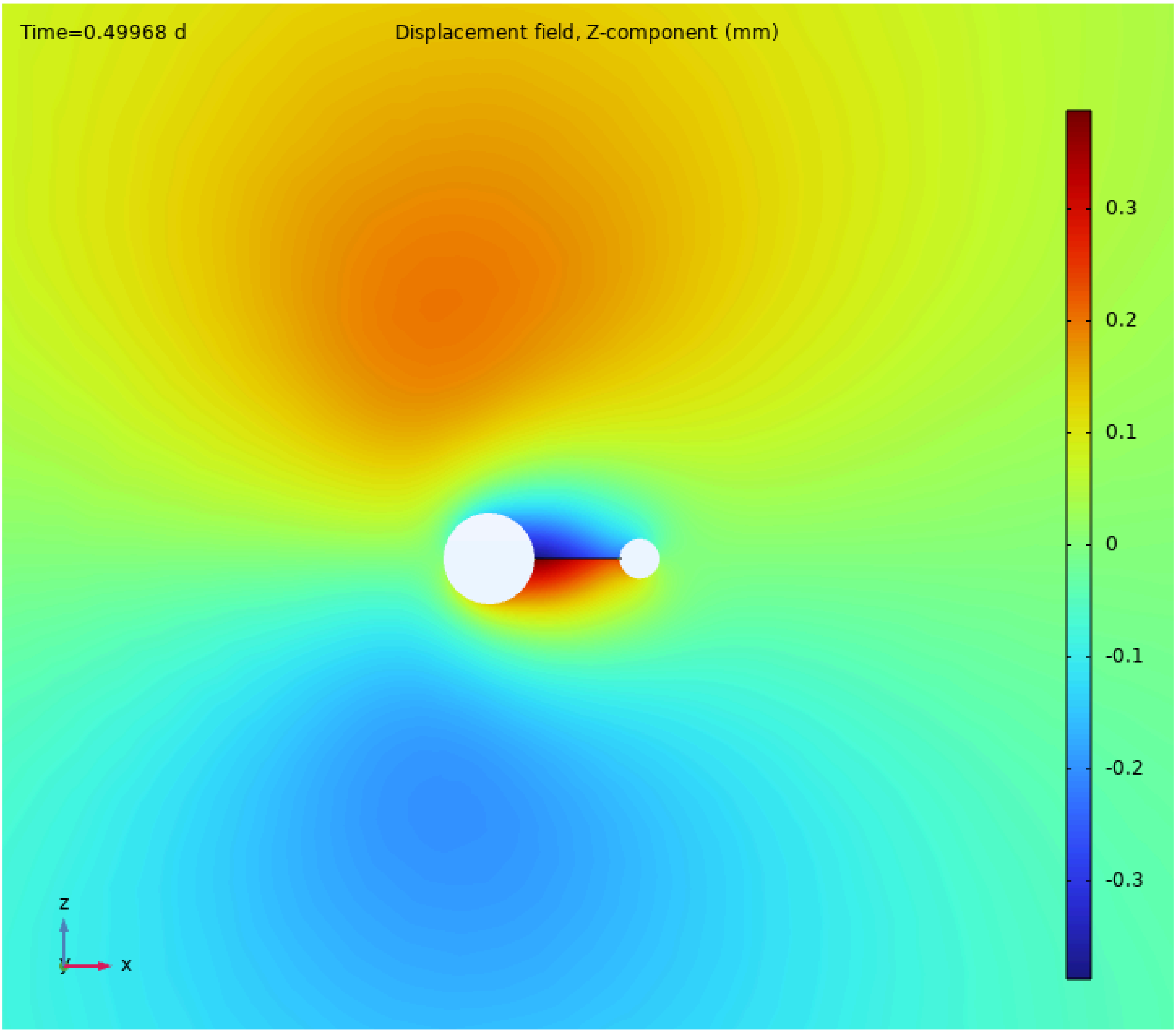

Figure A8. Z-component of the displacement field (mm) in the ZX-plane at the mid-height of the heater (y = 3 m), for the calibrated parameter set (R = 3.5, aperture = 0.0031 mm) with fracture length L = 1.84 m, at t = 0.5 days. Thermal expansion around the HP borehole (left) produces outward displacement, while the connecting fracture channel toward the D borehole (right) shows the resulting asymmetric deformation pattern. Additionally, most of the displacement is concentrated along the fracture, with amplitude increasing as distance from the HP borehole decreases.

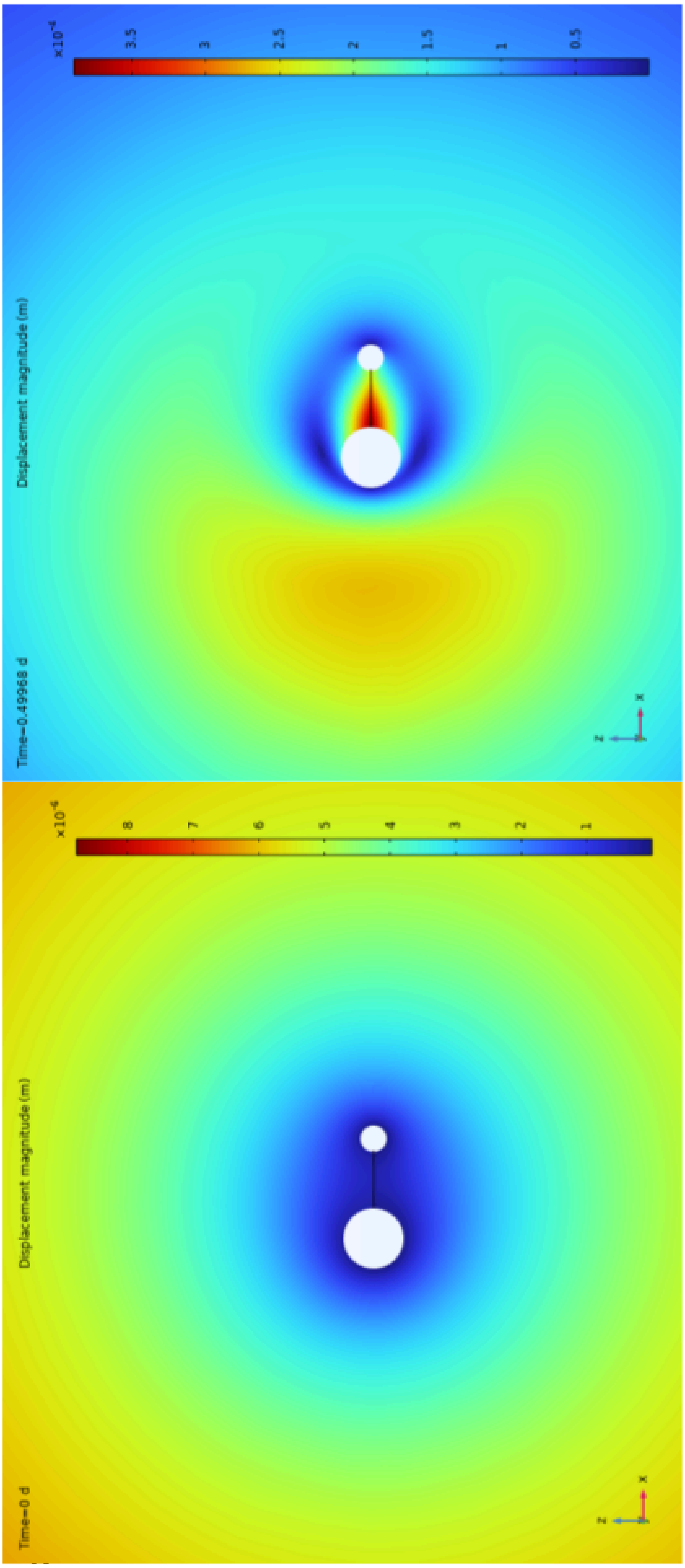

Figure A9. Displacement magnitude (m) in the ZX-plane at the mid-height of the heater, comparing the initial unheated state (t = 0 d, bottom) with the state after 0.5 days of heating (top), for R = 3.5, aperture = 0.0031 mm, L = 1.84 m. At t = 0, displacement is governed only by the small mechanical adjustment around the open boreholes, producing a weak, axisymmetric halo with no preferential direction. By t = 0.5 d, displacement peaks sharply at the HP borehole wall, where thermal expansion is greatest, and is elongated toward the D borehole along the fracture. This pattern indicates that mechanical stress propagates preferentially through the fracture rather than the surrounding undisturbed salt.

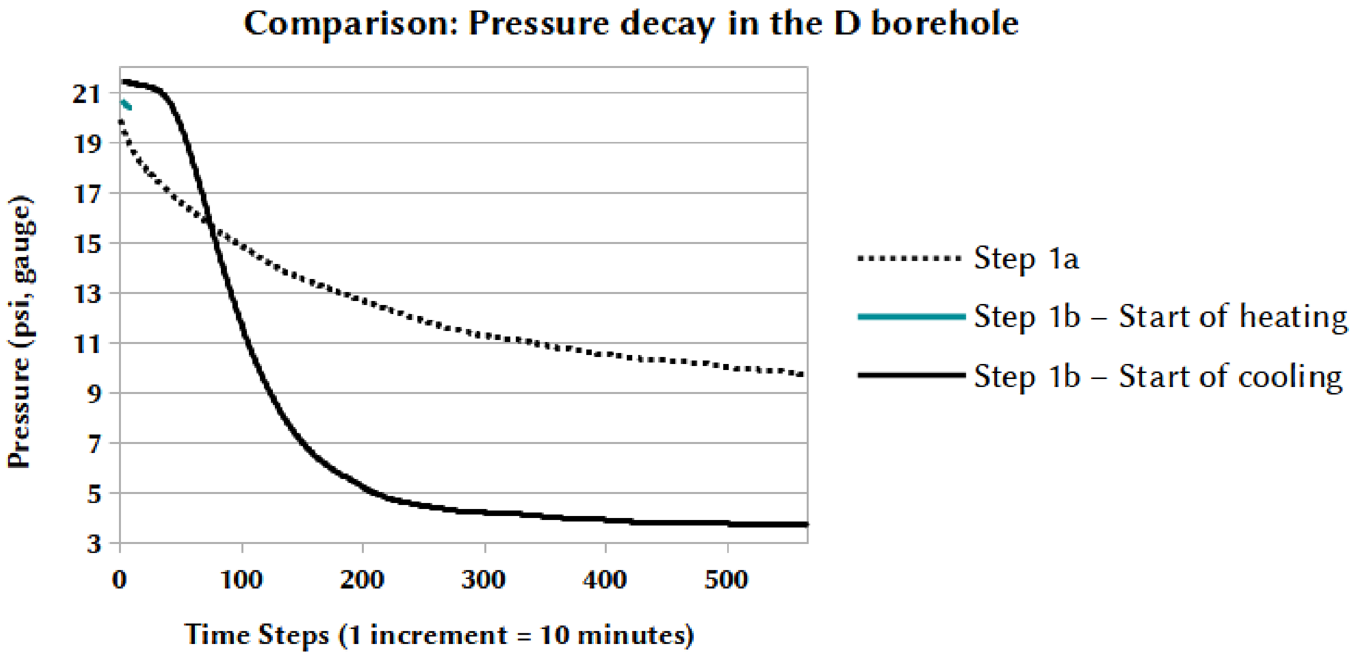

Figure A10. Comparison of the pressure decays in the D borehole at different times of the simulation that occurred in 2024. Step 1a here starts on the 30th of May (10 am) and ends on the 3rd of June (8:30 am); Step 1b (run A - blue line) begins on the 3rd of June (8:50 am) and ends that same day at 10:20 am. The last line (black and continuous) represents the pressure after the heater is turned off; it starts on the 29th of July 2024 at 10:20 am and ends on the 5th of August 2024 (8:10 am). There is a contrast between the early heating-onset pressure trend and the post-shutoff trend, bolstering the asymmetry between fracture closure and reopening.

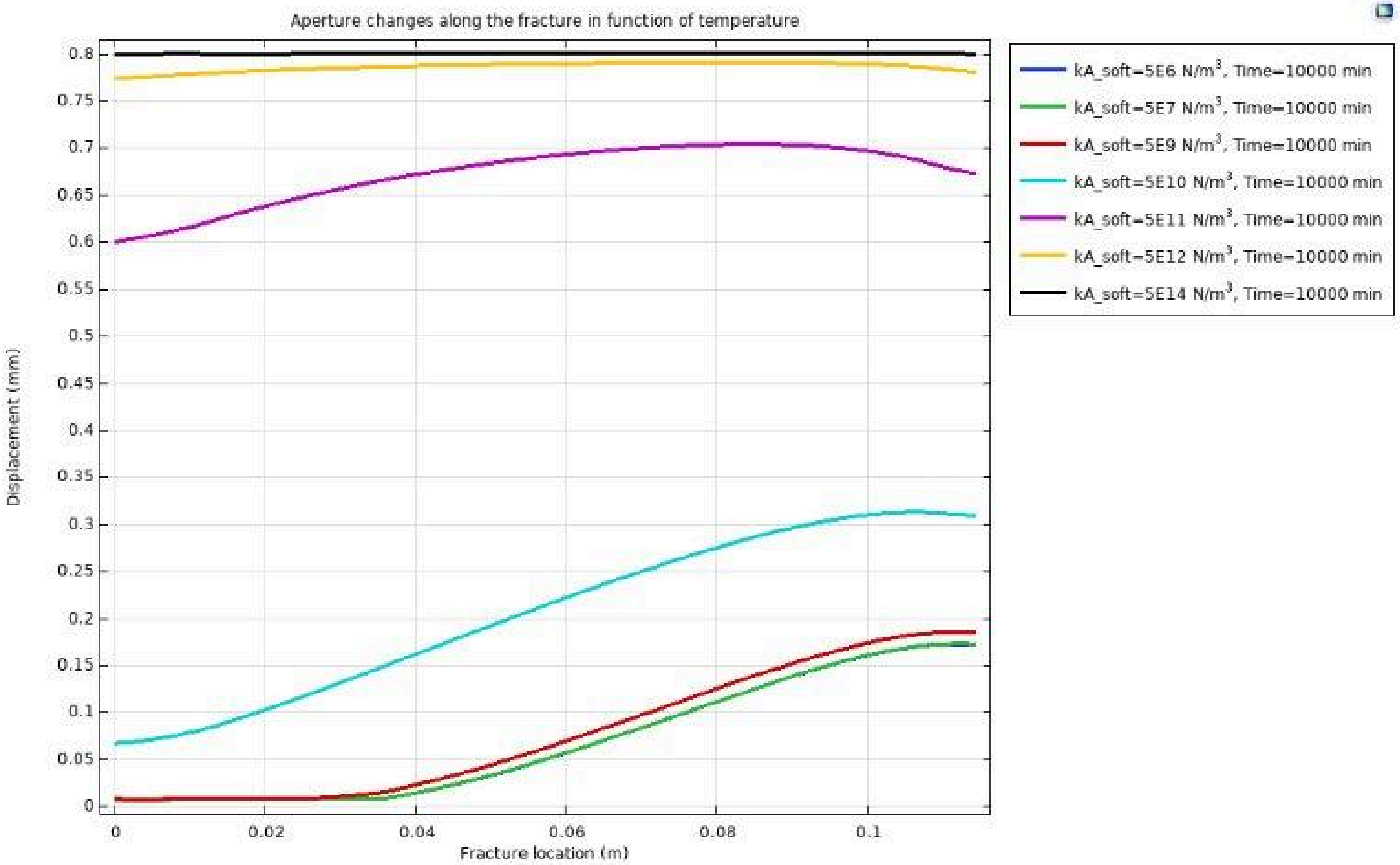

Figure A11: Parametric sweep of the mechanical spring stiffness (k_a) governing the thin-layer fracture formulation, showing fracture-face displacement as a function of position along the fracture after 10,000 minutes of heating at 600 W. The fracture position axis runs from the HP borehole contact (0 m) to the D borehole contact; results are shown for k_a ranging from $5 * 10^{6}\, to\, 5 * 10^{14} N/m^{3}$*, illustrating the sensitivity of aperture closure to the assumed spring stiffness.*

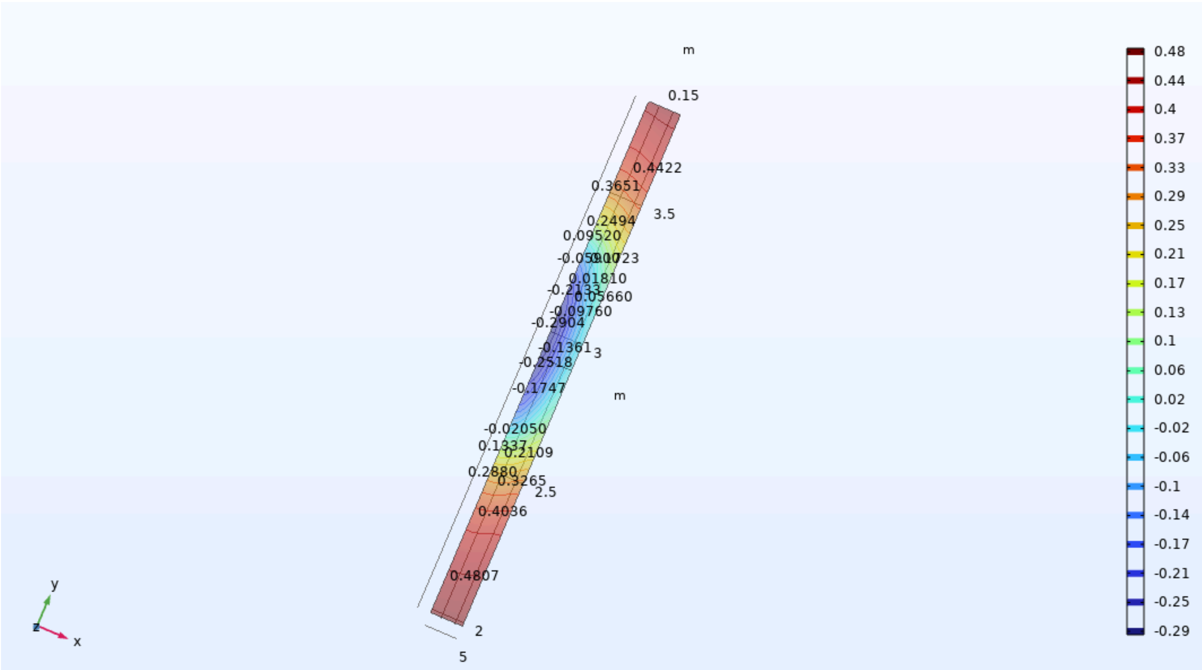

Figure A12: Non-uniform closure of the fracture, at t=1000 minutes, with a fracture length of 1.84m. The D borehole is to the right of this fracture, and the HP to the left. A negative value indicates an aperture size of 0 m. In this simulation, the initial aperture was 0.5 mm, close to the maximum possible aperture. The maximum aperture was first measured in preliminary stages of the project, in an intermediary 2D mechanical model. It was defined as 0.59mm (using the thermal coefficient $4.0 * 10^{-5} 1/K$*, a distance to the nearest constrained wall of 0.134 m, and a thermal gradient of 110K).*

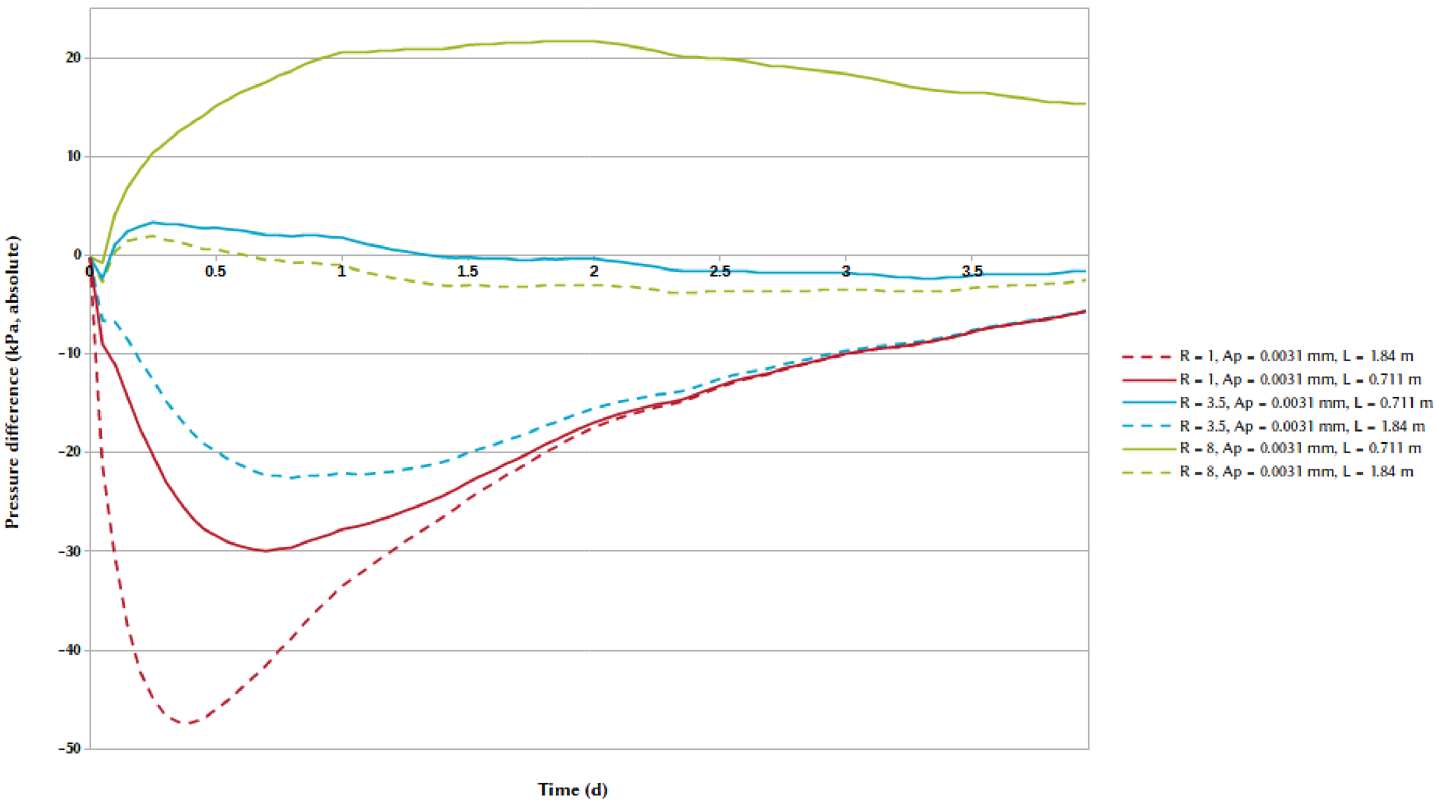

Figure A13: The difference in pressure decay in the D borehole (kPa, absolute) between the experimental results and the model results. The blue continuous line represents the best-fit set of parameters with the experimental data (Run A).

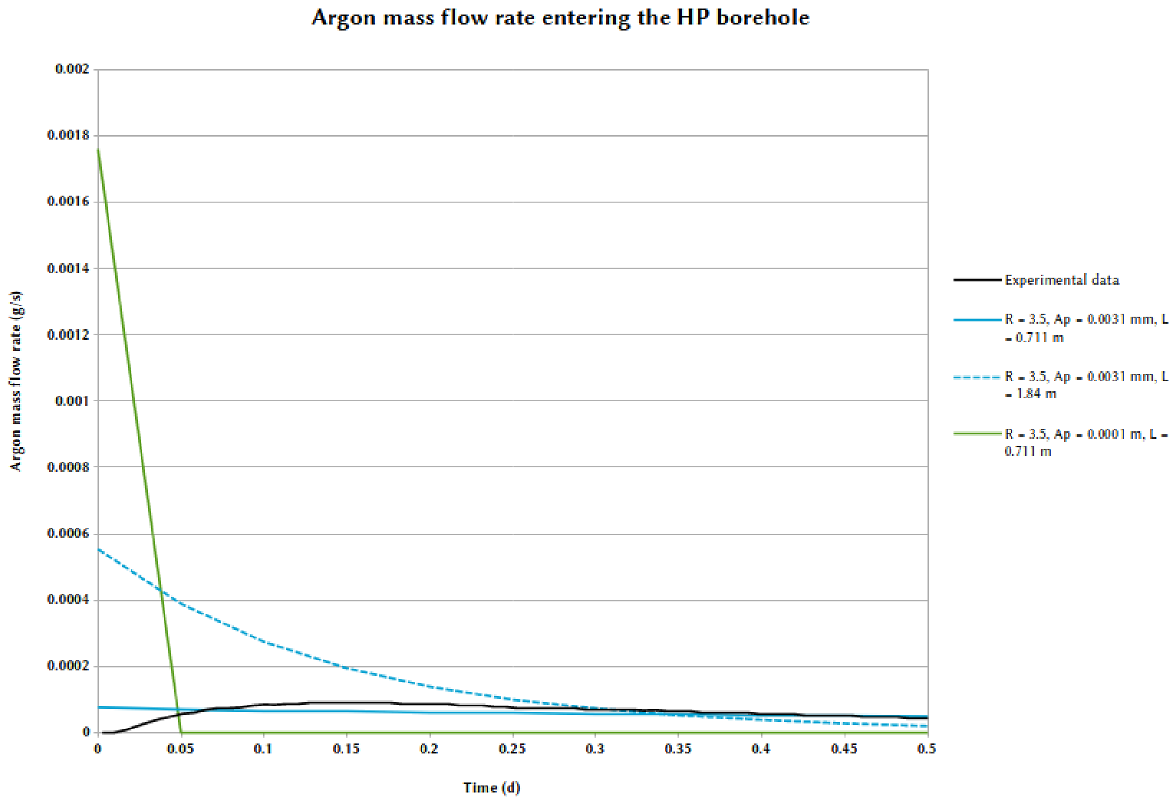

Figure A14: Mass flow rate of argon (g/s) entering the HP borehole from t=0 days to t=0.5 days. This figure is a zoom of Figure 8, to allow for better visualization of the results.

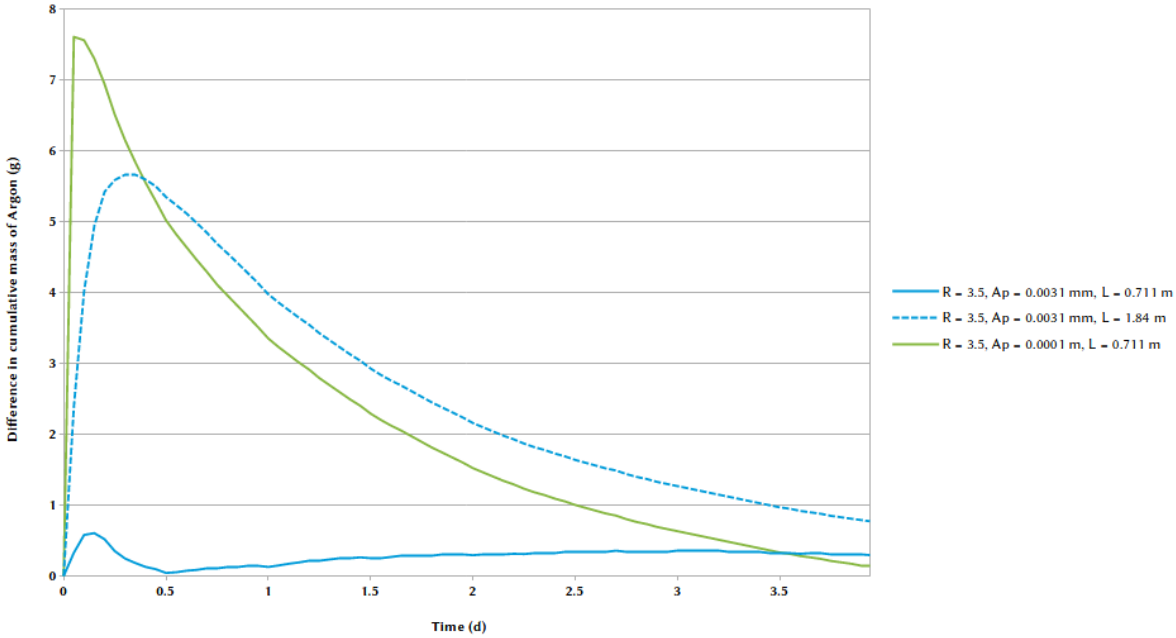

Figure A15: The difference in cumulative mass of argon in the HP borehole throughout Step 1b between the experimental results and the model results. The blue continuous line represents the best-fit set of parameters (Run A).

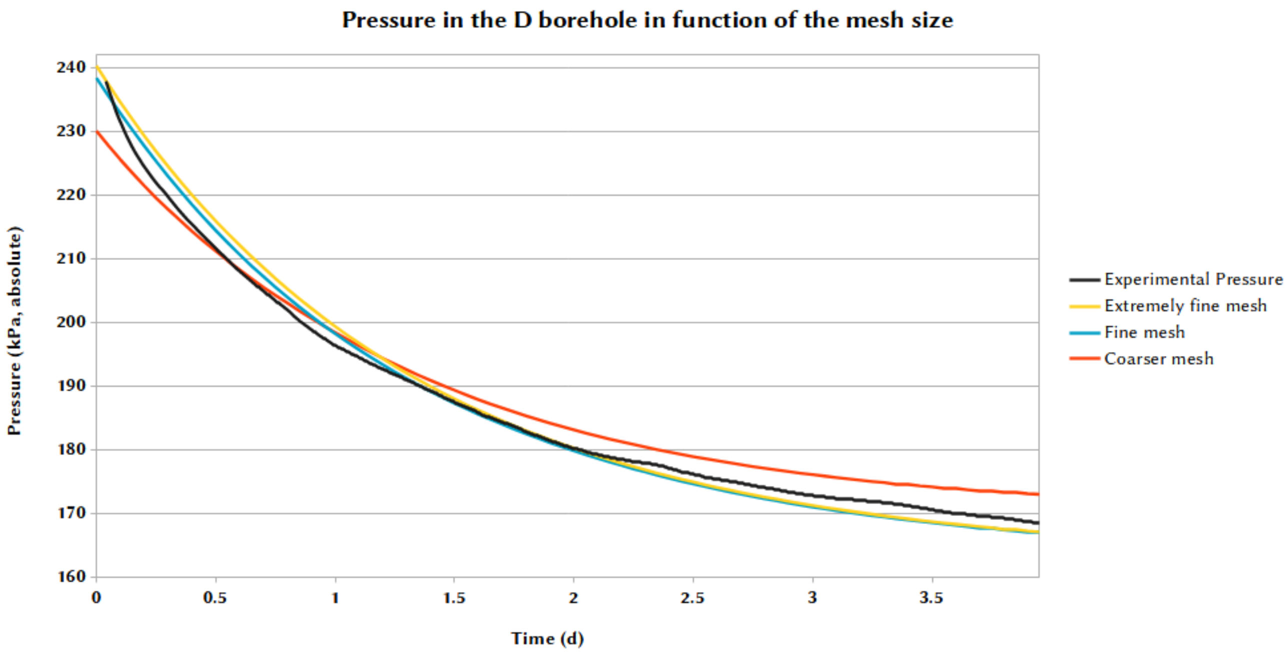

Figure A16: Pressure decay in the D borehole under ambient conditions (Step 1a) as a function of the mesh size given ted to the refined mesh zone around the two boreholes and fracture. A finer mesh size yields a more accurate t=0 pressure value, whereas coarsening the mesh size leads to an underestimation of the t=0 pressure and an overestimation of the pressure during the simulation.